# Covariance spectrum in nonlinear recurrent neural networks

Xuanyu Shen[1] and Yu Hu*[1,2]

[1]Department of Mathematics, The Hong Kong University of Science and Technology, Hong Kong SAR, China
[2]Division of Life Science, The Hong Kong University of Science and Technology, Hong Kong SAR, China

**Abstract**

Advances in simultaneous recordings of large numbers of neurons have driven significant interest in the structure of neural population activity such as dimension. A key question is how these dynamic features arise mechanistically and their relationship to circuit connectivity. It was previously proposed to use the covariance eigenvalue distribution, or spectrum, which can be analytically derived in random recurrent networks, as a robust measure to describe the shape of neural population activity beyond the dimension (Hu and Sompolinsky 2022). Applications of the theoretical spectrum have broadly found accurate matches to experimental data across brain areas providing mechanistic insights into the observed low dimensional population dynamics (Morales et al. 2023). However, the empirical success highlights a gap in theory, as the neural network model used to derive the spectrum was minimal with linear neurons. In this work, we aim to close this gap by studying the covariance spectrum in networks with nonlinear neurons and under broader dynamical regimes including chaos. Surprisingly, we found that the spectrum can be precisely understood by equations analogous to the linear theory substituted with an effective recurrent connection strength parameter, that reflects both the connection weights and the nonlinearity of neurons. Across dynamical regimes, this effective connection strength provides a unified interpretation for the spectrum and dimension changes, and stays near the critical value in the chaotic regime without fine-tuning. These results further our understanding of nonlinear neural population dynamics and provide additional theoretical support for applying the covariance spectrum analysis in biological circuits.

**Keywords:** neural population dynamics; recurrent neural network; network connectivity; nonlinear dynamics and chaos

## 1 Introduction

Understanding the relationship between neural dynamics and the underlying network connectivity is a central question in theoretical neuroscience and is also of common interest to other fields studying complex and extensively interacting systems. In recent years, there have been significant developments in large-scale simultaneous recordings of neural activity [2, 15, 25, 27], which not only increase the quantity of data but also allow for new ways of analyzing population activity structures at the multi-dimensional level, rather than averaging across neurons. Examples of such analyses include principal component analysis (PCA) [27], dimension [22, 5, 6], neural manifold [7],

*To whom correspondence should be addressed: mahy@ust.hk

communication subspace [25] among others. This, in turn, has driven intense interest in theoretical studies aimed at understanding how these properties of population dynamics arise mechanistically and relate to the network connectivity structure in neural circuit models [18, 23, 4, 11, 9].

In particular, the eigenvalues of the covariance matrix of neural activity, or the covariance spectrum [11], provide information about the shape of population activity beyond its dimension. This description of population dynamics is useful and has been applied to whole-brain neural activity to reveal a scale-invariance phenomenon [30]. Hu and Sompolinsky developed a theory [11] predicting the covariance spectrum in recurrent neural circuits, using simple models with random connections [26, 16] or with second-order motifs [31, 10], and linear neuronal dynamics. The theory has been found to match well with experimental data, including recordings from various brain regions, recording methods, and animal species [11, 19, 3]. By fitting the theoretical spectrum [11] to human Magnetoencephalography (MEG) data across frequency bands, Calvo et al. found that the fitted recurrent strength parameter can be used to distinguish Parkinson's disease patients from healthy controls [3].

However, the empirical success of the model covariance spectrum highlights a gap in theory, because biological neural networks are complex, and the assumptions made in [11] may not be sufficient to describe more complex *nonlinear dynamics* such as chaos [26, 16, 24]. It is technically challenging to determine correlations in chaotic states. For example, in the classic mean-field theory (MFT) of randomly connected networks, correlations between neurons were ignored [26], as they vanish in large networks as $O(1/\sqrt{N})$, where $N$ is the number of neurons. In a recent breakthrough, Clark et al. derived the leading-order correlations in terms of the four-point function by developing a two-site cavity method [4]. These results allow for computing the second moments of the covariance matrix eigenvalues and, in turn, for determining the participation ratio dimension [17, 22] of these randomly connected recurrent neural networks (RNNs) in chaotic states.

In this paper, we aim to close the aforementioned theoretical gap by determining the covariance spectrum in nonlinear randomly connected RNNs. This work builds on and extends the results of [11] and [4] to gain a more detailed understanding of population dynamics beyond its dimension in chaotic states and provide theoretical backing for applying covariance spectrum analysis to real data. A key step is proposing a closed-form ansatz for the covariance matrix (Eq. (3.3)), motivated and supported by theoretical and numerical evidence, particularly through comparisons with networks with linear neurons [11]. The (frequency-dependent) covariance spectrum, for both firing rates and currents, is then derived from these covariance matrix expressions.

To obtain a full picture of how the dynamics, described by the spectrum and dimension, change across dynamical regimes, especially during the transition to chaos [28], we have incorporated independent external inputs modeled as white noise into the network model [24]. Importantly, we found that the changes in covariance spectrum and dimension can be understood in a unified manner in terms of an effective recurrent connection strength parameter $g_{\text{eff}}$ (Eq. (3.2)). Moreover, we study how the gap between the dimension of firing rates and that of currents [4] changes along the transition to chaos and reveal a subtle relationship.

The rest of the paper is organized as follows. In Section 2, we introduce the recurrent network model and define the covariance matrix, participation ratio dimension, and covariance spectrum. In Section 3, we propose the ansatz for the covariance matrix and discuss its numerical and theoretical validations. In Section 4, we use the ansatz and its corollary to derive the covariance spectrum for firing rates and currents. In Section 5, we study the behavior of the effective recurrent connection strength $g_{\text{eff}}$ across dynamical regimes and investigate the relationship between the dimension gap and the transition to chaos.

## 2 Neural network model

We study the dynamics of a recurrent network of $N$ neurons, where the total current of neuron $i$, $x_i(t)$, evolves as

$$\frac{dx_i(t)}{dt} = -x_i + \sum_{j=1}^{N} J_{ij}\phi(x_j) + \xi_i(t), \quad i = 1, 2, \cdots, N. \tag{2.1}$$

The neurons are coupled by a random network (fixed during the neural dynamics) [26, 24, 11, 4], specified by the connectivity matrix $\mathbf{J} = (J_{ij})_{1\le i,j\le N}$, whose entries are drawn i.i.d. from a Gaussian distribution with zero mean and variance $g^2/N$. In particular, such a network is balanced on average in excitation and inhibition, and the parameter $g$ controls the recurrent connection strength. The nonlinear neuronal activation function $\phi(x) = \tanh(x)$ converts the neuron's current to its firing rate. For ease of notation, we write $\phi_i(t) = \phi(x_i(t))$. The neurons are also driven by external inputs $\xi_i(t)$ that are independent across neurons $i$ and are modeled as Gaussian white noise with strength $\sigma$, such that $\langle \xi_i(t)\xi_j(t+\tau)\rangle = \sigma^2\delta_{ij}\delta(\tau)$. We use the notation $\langle\cdot\rangle := \mathbb{E}_t[\cdot]$ to denote the temporal average over the stochastic input.

We are interested in the population dynamics of the network described by the covariance matrix and related quantities. In particular, the time-lagged covariance, or correlation function, between neurons $i$ and $j$ is $C^x_{ij}(\tau) = \langle \Delta x_i(t)\Delta x_j(t+\tau)\rangle$, $C^\phi_{ij}(\tau) = \langle \Delta\phi_i(t)\Delta\phi_j(t+\tau)\rangle$, where $\Delta x_i = x_i - \langle x_i\rangle$, $\Delta\phi_i = \phi_i - \langle\phi_i\rangle$. Due to symmetry, $\langle x_i\rangle = \langle\phi_i\rangle = 0$, so we drop the $\Delta$ notation in writing covariances. Note that we have two covariance matrices $\mathbf{C}^a(\tau) = (C^a_{ij}(\tau))$, $a \in \{x, \phi\}$ for the currents and firing rates, respectively. More generally we use notations such as $\mathbf{C}^{x\phi}(\tau) = (C^{x\phi}_{ij}(\tau)) = (\langle x_i(t)\phi_j(t+\tau)\rangle)$ to denote the cross-covariance. We assume the dynamics is stationary so the covariance depends only on the time delay $\tau$. The covariance matrices can also be equivalently described in the frequency domain by performing an entry-wise Fourier transform $C^a_{ij}(\omega) = \mathcal{F}\left[C^a_{ij}(\tau)\right] := \int_{-\infty}^{\infty} e^{-i\omega\tau} C^a_{ij}(\tau)d\tau$ to obtain the frequency-dependent covariance matrices $\mathbf{C}^a(\omega) = (C^a_{ij}(\omega))$. For ease of notation, we write the zero time lag covariance matrix as $\mathbf{C}^{a,\tau} = \mathbf{C}^a(\tau = 0)$ and the zero-frequency covariance matrix as $\mathbf{C}^{a,\omega} = \mathbf{C}^a(\omega = 0)$. Similar notations are used for $\phi$, $\eta$, and other related quantities including dimensions.

The structure of neuron population activity or dynamics can then be characterized in terms of dimension and shape. Specifically, the (relative) participation ratio dimension [22, 17, 23] can be calculated from the covariance matrix as $D(\mathbf{C}) = \frac{1}{N}\frac{\left(\sum_{i=1}^N \lambda_i\right)^2}{\sum_{i=1}^N \lambda_i^2}$, where $\lambda_i$ are eigenvalues of the covariance matrix $\mathbf{C}$. Here $D$ is normalized by the number of neurons and thus lies within $[0, 1]$. The covariance spectrum additionally describes the shape besides the dimension, of the population activity [11, 30], is the probability density function of the covariance eigenvalues, whose empirical distribution $p(\lambda) = \frac{1}{N}\sum_{i=1}^N \delta(\lambda - \lambda_i)$ may converge to a continuous function in the large network limit $N \to \infty$ that can be determined from the model parameters, such as the recurrent connection strength $g$ [11].

With the nonlinear neurons, the network can be in different dynamical regimes, including chaos, depending on the model parameters $(g, \sigma)$ (Fig. 2A, [24]). For a fixed $\sigma > 0$, as we increase the recurrent connection strength $g$ until a value $g_{c_1}$, the network switches from stable fluctuations around a fixed point (linearly stable regime) to a regime where the Jacobian matrix characterizing the linear stability has eigenvalues with positive real parts (linearly unstable regime) [24]. Despite the linear instability, the dynamics is not yet chaotic, which is characterized by a positive leading Lyapunov exponent and occurs at a larger $g = g_{c_2}$. Importantly, due to the presence of fluctuating input $\xi_i(t)$ requires a larger $g_{c_2}$ than the autonomous or noiseless case of $\sigma = 0$ where $g_{c_2} = 1$ (and without the linear unstable regime) [26, 24]. The critical values $g_{c_1}$ and $g_{c_2}$ can be determined using

a mean-field theory focusing on a single, typical neuron [24, 26]. For example, $g_{c_1} = 1/\sqrt{\left\langle [\phi'(x)]^2 \right\rangle}$ [24]. Note that we dropped the neuron index in the above expression and in other places such as $C^x(\tau)$ for the autocorrelation function instead of $C^x_{ii}(\tau)$. This is justified because neurons become homogeneous or equivalent to each other in the large network limit $N \to \infty$. The transition value $g_{c_2}$ for chaos, and statistics such as $C^a(\tau)$ and $\langle \phi' \rangle = \langle \phi'(x_i(t)) \rangle$, can be determined from a mean-field equation for a single neuron's dynamics [26, 24],

$$(1+\omega^2) C^x(\omega) = g^2 C^\phi(\omega) + \sigma^2, \tag{2.2}$$

which stems from analyzing the statistics of the total recurrent input to a neuron $\eta_i(t) := \sum_{j=1}^N J_{ij}\phi_j(t)$ over the ensemble of the random connectivity $\mathbf{J}$.

## 3 Covariance matrix ansatz

To achieve our goal of characterizing the shape of neural population activity using the covariance spectrum, we need a description of the covariance matrix. In particular, the lower order statistics of $C^a_{ij}$ although they can be used to derive the dimension $D$ [4, 23], are not sufficient for the spectrum. Here we propose a guess or ansatz for the covariance matrix $\mathbf{C}^\phi(\omega)$ based on a crucial observation that the frequency-dependent dimension $D^\phi(\omega) := D(\mathbf{C}^\phi(\omega))$ has a simple expression (Eq. (3.1)) closely related to the linear dynamics counterpart. Although as we elaborate below, $D^\phi(\omega)$ can be readily derived from [4], and the linear dimension and spectrum theory have been empirically applied to potentially strongly nonlinear networks [11, 19, 3], this connection between the nonlinear and linear network dynamics has not been explicitly made to the best of our knowledge.

As a slight extension of the result on dimension in [4], which focuses on the case without external input $\sigma = 0$, we derive the frequency-dependent dimension $D^\phi(\omega)$ for $\sigma \geq 0$ valid for all values of $g$, by computing the four-point function $\psi^\phi(\omega) := N \left\langle C^\phi_{ij}(\omega) C^\phi_{ij}(-\omega) \right\rangle_{\mathbf{J}} \Big|_{i \neq j}$ following a similar two-site cavity mean-field theory in [4] (Appendix B). Importantly, a factor of the single neuron dynamics quantity $\left[C^\phi(\omega)\right]^2$ appearing in both the first and second moments of covariance eigenvalues cancels when computing the dimension,

$$D^\phi(\omega) = \left(1 - \frac{g^2 \langle \phi' \rangle^2}{1+\omega^2}\right)^2. \tag{3.1}$$

This simple expression takes an analogous form to the dimension of the linear network [11], $D_{\text{lin}}(\omega) = \left(1 - \frac{g^2}{1+\omega^2}\right)^2$. In particular, if we replace $g$ with an *effective recurrent connection strength* ([4], see further discussions in Section 5 including that it is always less than 1),

$$g_{\text{eff}} = g \left\langle \phi' \right\rangle, \tag{3.2}$$

then the nonlinear dynamics dimension $D^\phi(\omega)$ matches with $D_{\text{lin}}(\omega)$ across all frequencies $\omega$. This motivates to propose an ansatz for the firing rate covariance matrix under nonlinear dynamics,

$$\text{Ansatz:} \quad \mathbf{C}^\phi(\omega) = \frac{C^\phi(\omega)(1 - g^2 \langle \phi' \rangle^2 + \omega^2)}{1+\omega^2} \left(\mathbf{I} - \frac{\langle \phi' \rangle}{1+i\omega}\mathbf{J}\right)^{-1} \left(\mathbf{I} - \frac{\langle \phi' \rangle}{1-i\omega}\mathbf{J}^T\right)^{-1}. \tag{3.3}$$

Here $\mathbf{I}$ is the identity matrix. The ansatz is based on the counterpart in a linear dynamics network driven by independent white noise $\mathbf{C}_{\text{lin}}(\omega) = \frac{\sigma^2}{1+\omega^2}\left(\mathbf{I} - \frac{1}{1+i\omega}\mathbf{J}\right)^{-1}\left(\mathbf{I} - \frac{1}{1-i\omega}\mathbf{J}^T\right)^{-1}$ [11, 29, 8]. The scalar factor in Eq. (3.3) ensures the two sides match at the first moment (Appendix C).

### 3.1 Covariance matrix of currents $\mathbf{C}^x(\omega)$

As noted in [4], the firing rate and current covariances are different, and for example, they have different dimensions $D^\phi$ and $D^x$. To derive the covariance matrix for currents $\mathbf{C}^x(\omega)$, we start by taking the Fourier transform of the neural dynamics equation (Eq. (2.1)), $\boldsymbol{x}(\omega) = \frac{1}{\sqrt{T}}\int_0^T e^{-i\omega t}\boldsymbol{x}(t)dt$, $\boldsymbol{x} = (x_i)_{i=1}^N$ and multiply it by its conjugate transpose to obtain $\mathbf{C}^x(\omega) = \lim_{T\to\infty}\left\langle \boldsymbol{x}(\omega)\boldsymbol{x}^\dagger(\omega)\right\rangle$ (Wiener-Khinchin theorem),

$$(1+\omega^2)\mathbf{C}^x(\omega) = \mathbf{J}\mathbf{C}^\phi(\omega)\mathbf{J}^T + \mathbf{J}\mathbf{C}^{\phi\xi}(\omega) + \mathbf{C}^{\xi\phi}(\omega)\mathbf{J}^T + \sigma^2\mathbf{I}. \tag{3.4}$$

Here $\boldsymbol{x}^\dagger$ represents the conjugate transpose of the vector $\boldsymbol{x}$. Without external inputs $\sigma = 0$, this combined with the $\mathbf{C}^\phi(\omega)$ ansatz (Eq. (3.3)) immediately gives an expression for $\mathbf{C}^x(\omega)$.

For the case with external inputs, in the large network limit, $x_i(t)$ becomes a Gaussian process according to the classic mean-field arguments [26]. Moreover, $(x_i(t), \xi_j(t+\tau))$ are jointly Gaussian distributed in this limit. Then by Stein's lemma, we have $\langle\phi(x_i(t))\xi_j(t+\tau)\rangle = \langle\phi_i'\rangle\langle x_i(t)\xi_j(t+\tau)\rangle$. Taking the Fourier transform and writing in a matrix form, this gives

$$\mathbf{C}^{\phi\xi}(\omega) = \mathbf{D}_{\langle\phi'\rangle}\mathbf{C}^{x\xi}(\omega), \tag{3.5}$$

where $\mathbf{D}_{\langle\phi'\rangle} = \mathrm{diag}(\langle\phi_1'\rangle, \langle\phi_2'\rangle, \ldots, \langle\phi_N'\rangle)$ is a diagonal matrix. On the other hand, substituting $\boldsymbol{x}$ in $\mathbf{C}^{x\xi}(\omega)$ using the dynamics equation Eq. (2.1) gives

$$\mathbf{C}^{x\xi}(\omega) = \frac{1}{1+i\omega}\left[\mathbf{J}\mathbf{C}^{\phi\xi}(\omega) + \sigma^2\mathbf{I}\right]. \tag{3.6}$$

We can now solve for $\mathbf{C}^{\phi\xi}(\omega)$ from Eqs. (3.5) and (3.6) and plug it into Eq. (3.4) to get (Appendix D),

$$\begin{aligned}\mathbf{C}^x(\omega) = {} & \frac{C^\phi(\omega) - \langle\phi'\rangle^2 C^x(\omega)}{1+\omega^2}\mathbf{J}\left(\mathbf{I} - \frac{\langle\phi'\rangle}{1+i\omega}\mathbf{J}\right)^{-1}\left(\mathbf{I} - \frac{\langle\phi'\rangle}{1-i\omega}\mathbf{J}^T\right)^{-1}\mathbf{J}^T \\ & + \frac{\sigma^2}{1+\omega^2}\left(\mathbf{I} - \frac{\langle\phi'\rangle}{1+i\omega}\mathbf{J}\right)^{-1}\left(\mathbf{I} - \frac{\langle\phi'\rangle}{1-i\omega}\mathbf{J}^T\right)^{-1}.\end{aligned} \tag{3.7}$$

Here we have replaced $\mathbf{D}_{\langle\phi'\rangle}$ with $\langle\phi'\rangle\mathbf{I}$ because in the large network limit $N\to\infty$, neuronal dynamics become homogeneous. Comparing with linear dynamics theory [11], the above expression intuitively bridges the theory of linear and chaotic dynamics (see also Eq. (3.13)). The first term in Eq. (3.7) represents the contribution from nonlinear dynamics such as chaos (see Eq. (3.13)) and causes $\mathbf{C}^x$ to differ from $\mathbf{C}^\phi$. This term is zero when the neurons are linear, $\phi(x) = x$, in which case only the second term corresponding to external noise input remains.

### 3.2 Interpretation and numerical supports

Here we provide some intuitive explanations of the covariance matrix ansatz along with numerical verifications. We want to emphasize that the covariance matrix expressions (Eqs. (3.3) and (3.7)) hold for each individual realization of the network connectivity $\mathbf{J}$, rather than only describing the covariance matrices on a statistical level over the distributions of the random $\mathbf{J}$. This is verified by direct simulations of the nonlinear network (Fig. 1A,B). For a fixed $\mathbf{J}$, the theoretical covariance matrices computed using Eqs. (3.3) and (3.7) and the mean-field quantities match closely with those computed from simulated neural activity, and the relative error between the theory and simulation decreases with the network size $N$ (Fig. 1C,D).

The covariance matrix ansatz (Eq. (3.3)) has a heuristic explanation by introducing an effective noise. For simplicity, we first explain this for the case without external input $\sigma = 0$. Define the *effective recurrent noise* as

$$\zeta_i := \phi_i - \langle \phi_i' \rangle x_i. \tag{3.8}$$

We can compute the variance of $\zeta_i$ in the frequency domain. According to the classic mean-field theory, $\{x_i(t)\}_t$ is a Gaussian process [26], therefore $\langle x_i(\omega)\phi_i^*(\omega)\rangle = \langle \phi_i' \rangle \langle x_i(\omega)x_i^*(\omega)\rangle$ by the Stein's lemma. Then using Eq. (3.8), $\langle \zeta_i(\omega)\zeta_i^*(\omega)\rangle = \langle \phi_i(\omega)\phi_i^*(\omega)\rangle - \langle \phi_i' \rangle [\langle x_i(\omega)\phi_i^*(\omega)\rangle + \langle \phi_i(\omega)x_i^*(\omega)\rangle] + \langle \phi_i' \rangle^2 \langle x_i(\omega)x_i^*(\omega)\rangle = \langle \phi_i(\omega)\phi_i^*(\omega)\rangle - \langle \phi_i' \rangle^2 \langle x_i(\omega)x_i^*(\omega)\rangle$. Note that the neuron index $i$ can be dropped due to the homogeneity of neurons as $N \to \infty$. Then the Fourier transform of the autocorrelation function of $\zeta$, or $C^\zeta(\omega)$, is

$$C^\zeta(\omega) = C^\phi(\omega) - \langle \phi' \rangle^2 C^x(\omega) = \left(1 - \frac{g^2 \langle \phi' \rangle^2}{1+\omega^2}\right) C^\phi(\omega). \tag{3.9}$$

Here we used the mean-field relationship Eq. (2.2) (with $\sigma = 0$) to obtain the second equality.

We can use $\boldsymbol{\zeta} = (\zeta_i)$ to express $\boldsymbol{\phi}$. Plugging in the Fourier transform of the dynamics equation (Eq. (2.1)) into Eq. (3.8) gives $\zeta_i(\omega) = \phi_i(\omega) - \frac{\langle \phi_i' \rangle}{1+i\omega} \sum_{j=1}^N J_{ij}\phi_j(\omega)$. In matrix form, we can solve for $\boldsymbol{\phi}$,

$$\boldsymbol{\phi}(\omega) = \left[\mathbf{I} - \frac{1}{1+i\omega}\mathbf{D}_{\langle \phi' \rangle}\mathbf{J}\right]^{-1} \boldsymbol{\zeta}(\omega). \tag{3.10}$$

The covariance matrix of $\boldsymbol{\phi}$ is then (again invoking the homogeneity of neurons as $N \to \infty$),

$$\mathbf{C}^\phi(\omega) = [\mathbf{I} - \mathbf{J}_\mathrm{e}]^{-1} \mathbf{C}^\zeta(\omega) \left[\mathbf{I} - \mathbf{J}_\mathrm{e}^\dagger\right]^{-1}, \quad \text{where } \mathbf{J}_\mathrm{e} := \frac{\langle \phi' \rangle}{1+i\omega}\mathbf{J}. \tag{3.11}$$

Comparing this with Eq. (3.3), we see that our previous ansatz for $\mathbf{C}^\phi(\omega)$ can be justified if $\mathbf{C}^\zeta(\omega)$ is a scalar matrix,

$$\text{Ansatz:} \quad \mathbf{C}^\zeta(\omega) = C^\zeta(\omega) \cdot \mathbf{I} \quad \text{as } N \to \infty. \tag{3.12}$$

This means that $\zeta_i$ are independent and homogeneous across neurons $i$, and the scalar value of $C^\zeta(\omega)$ is given by Eq. (3.9).

In the general case with external inputs, the total effective noise to neuron $i$ will be $\tilde{\zeta}_i = \zeta_i + \frac{\langle \phi_i' \rangle}{1+i\omega}\xi_i$, which will replace $\zeta_i$ in Eq. (3.10). The rest of the argument can be generalized accordingly (Appendix E). In particular, in the large network limit $N \to \infty$, $\zeta_i$ are homogeneous and independent across neurons $i$, and are independent with the external noise $\boldsymbol{\xi}$. The covariance of currents (Eq. (3.7)) can be written using $C^\zeta(\omega)$,

$$\mathbf{C}^x(\omega) = \frac{C^\zeta(\omega)}{\langle \phi' \rangle^2}\mathbf{J}_\mathrm{e}(\mathbf{I} - \mathbf{J}_\mathrm{e})^{-1}\left(\mathbf{I} - \mathbf{J}_\mathrm{e}^\dagger\right)^{-1}\mathbf{J}_\mathrm{e}^\dagger + \frac{\sigma^2}{1+\omega^2}(\mathbf{I} - \mathbf{J}_\mathrm{e})^{-1}\left(\mathbf{I} - \mathbf{J}_\mathrm{e}^\dagger\right)^{-1}. \tag{3.13}$$

According to the ansatz (Eq. (3.12)), the off-diagonal entries of $\mathbf{C}^\zeta(\omega)$ should vanish in the large network limit. This is consistent with numerical simulations of the nonlinear network, where we find the off-diagonal entries of the sample estimated $\mathbf{C}^\zeta$ are much smaller relative to its diagonal (Fig. 1E). In other words, the average magnitude of correlations is small ($\overline{|\rho|} \approx 0.0057$). Moreover, this is drastically smaller than the $\overline{|\rho|} \approx 0.069$ of $\mathbf{C}^\phi$ (Fig. 1A,E). To further check the collective effect of $\mathbf{C}^\zeta$ off-diagonal entries, we compute its eigenvalues. If $\zeta_i$ are indeed independent across $i$ or sufficiently close to, these sample covariance matrix eigenvalues would be described by the Marchenko-Pastur law. This is indeed the case in our simulations (Fig. 1F).

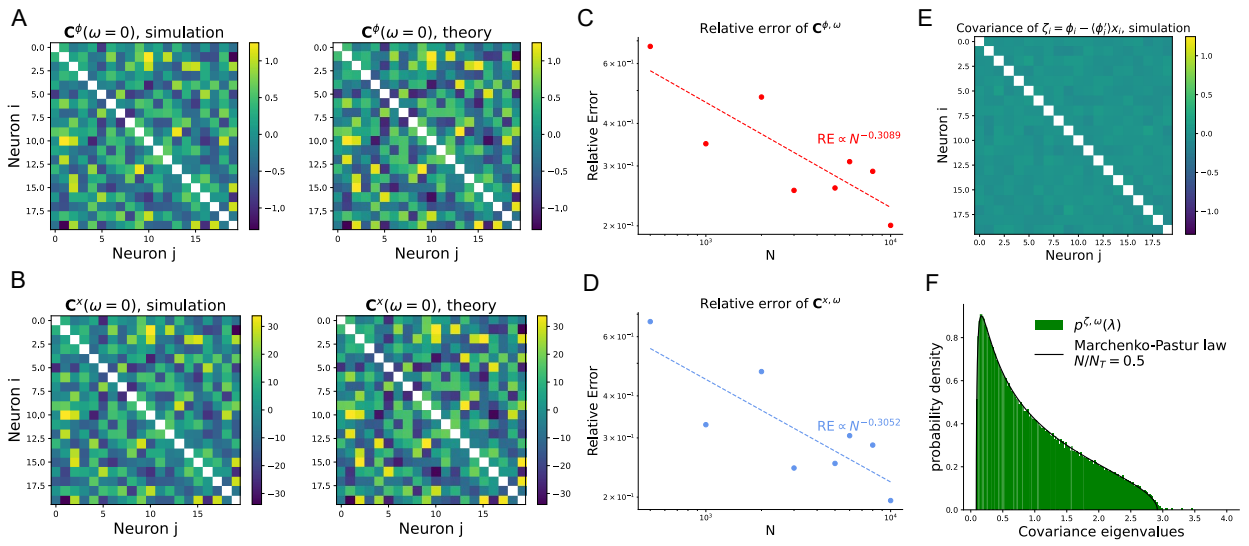


Figure 1: (**A**) Comparing the zero-frequency covariance matrix of firing rates $\mathbf{C}^{\phi,\omega}$ from network simulations (Eq. (2.1), left) with the ansatz (Eq. (3.3), right) for a subset of 20 neurons in a network with $N = 10000$ (under a single realization of connectivity $\mathbf{J}$). Diagonals are not shown to better visualize the off-diagonal entries. The network is in the chaotic regime with $g = 5$, $\sigma = 0.495$ (Fig. 2). (**B**) Same as (A), but comparing the covariance matrix for currents $\mathbf{C}^{x,\omega}$ from simulation and theory (Eq. (3.7), right) (**C, D**) Relative error between simulation and theory for $\mathbf{C}^{\phi,\omega}$ and $\mathbf{C}^{\zeta,\omega}$ (in Frobenius norm) decreases with the network size $N$. (**E**) Covariance matrix $\mathbf{C}^{\zeta,\omega}$ estimated from simulation (for the same 20 neurons as in (A) and (B)). The relative magnitude of its off-diagonal entries is quantified by $\overline{|\rho|} = \frac{1}{N(N-1)/2}\sum_{i<j}|C_{ij}|/\sqrt{C_{ii}C_{jj}}$, which is 0.0057. The matrix is scaled such that it has the same average diagonal values as $\mathbf{C}^{\phi,\omega}$ in (A) and is shown under the same color map to allow visual comparison of $\zeta$ and $\phi$ off-diagonal entries (with the latter has a much larger $\overline{|\rho|} = 0.069$). (**F**) The spectrum of the sample covariance matrix $\mathbf{C}^{\zeta,\omega}$ (computed from $N_T = 2N$ time samples (Appendix K) matches closely with the Marchenko-Pastur law expected for i.i.d. $\zeta_i$'s.

### 3.3 Theoretical validation based on dimension

As a validation of our covariance matrix expression for $\mathbf{C}^{x}(\omega)$ (Eq. (3.7)), we use it to provide an alternative derivation of the dimension $D^{x}(\omega)$ previously obtained in [4]. It is important to note that we did not use $D^{x}(\omega)$ and related moments in deriving Eq. (3.7) based on the $\mathbf{C}^{\phi}(\omega)$ ansatz, therefore the derivation of dimension is indeed a validation rather than a tautology.

Note that the moments of the eigenvalues can be computed using the trace of the covariance matrix powers. In particular, define $\varphi[\cdot] \coloneqq \lim_{N\to\infty}\frac{1}{N}\mathrm{Tr}\,\langle\cdot\rangle_{\mathbf{J}}$, where $\langle\cdot\rangle_{\mathbf{J}}$ denotes averaging over the realizations of the random connectivity $\mathbf{J}$. Then the $n$-th moment of the eigenvalues of $\mathbf{A}$ is $\varphi_n[\mathbf{A}] \coloneqq \varphi[\mathbf{A}^n]$. First, if we compute the first moment $\varphi[\cdot]$ on both sides of Eq. (3.7), we recover the mean-field theory for the diagonal entry or autocorrelation $C^{x}(\omega)$ (Eq. (2.2); derivations in Appendix D). Similarly, further computing the second moment $\varphi_2[\cdot]$ of Eq. (3.7) gives the (frequency-dependent) dimension of $x$,

$$D^{x}(\omega) = \frac{\left(\varphi_1\left[\mathbf{C}^{x}(\omega)\right]\right)^2}{\varphi_2\left[\mathbf{C}^{x}(\omega)\right]} = \frac{\left(1+\omega^2-g^2\left\langle\phi'\right\rangle^2\right)^2}{\left(1+\omega^2\right)^2+\left(1+\omega^2-\frac{\sigma^2}{C^{x}(\omega)}\right)^2-g^4\left\langle\phi'\right\rangle^4}. \tag{3.14}$$

Interestingly, when setting $\sigma = 0$, Eq. (3.14) readily reduces to exactly the same result previously derived in [4], albeit here we derive it using random matrix theory (Appendix D) which is a quite different approach from the two-site cavity method used in [4] (Appendix B).

In sum, supported by multifaceted theoretical and numerical evidence (Fig. 1 and Sections 3.2 and 3.3), we hypothesize that the proposed covariance matrix expressions Eqs. (3.3) and (3.7) are asymptotically exact in the large network limit of $N \to \infty$, across dynamical regimes including chaos.

## 4 Covariance spectrum

We are now ready to study the spectrum of the covariance matrices $\mathbf{C}^{\phi}(\omega)$ and $\mathbf{C}^{x}(\omega)$, which describe additional information of the shape of neural population activity beyond the dimension. The ansatz for $\mathbf{C}^{\phi}(\omega)$ (Eq. (3.3)) directly indicates that we can describe its (frequency-dependent) spectrum $p^{\phi}(\lambda;\omega)$ using the expression for the spectrum under linear dynamics $p_{\text{lin}}(\lambda;\omega)$ (Eq. 5 and 20 in [11]) by substituting $g$ with $g_{\text{eff}}$ (Eq. (3.2)),

$$p^{\phi}(\lambda;\omega,g,\sigma) = p_{\text{lin}}(\lambda;\omega,g_{\text{eff}},\sigma_{\text{eff}}(\omega)), \tag{4.1}$$

where $g_{\text{eff}} = g\langle\phi'\rangle$ (Eq. (3.2)) and $\sigma^2_{\text{eff}}(\omega) = (1-g^2\langle\phi'\rangle^2+\omega^2)C^{\phi}(\omega) = (1+\omega^2)C^{\tilde{\zeta}}(\omega)$ (see Section 3.2 and Appendix E).

For the covariance matrix of currents $\mathbf{C}^{x}(\omega)$, Eq. (3.7) also allows us to determine its spectrum in terms of network parameters. In particular, once $\langle\phi'\rangle$ and $C^{\phi}(\omega)$ are determined by the mean-field theory given parameters $g$ and $\sigma$ ([24], Eq. (2.2)), determining the spectrum of $\mathbf{C}^{x}(\omega)$ becomes a random matrix problem, albeit an involved one. Here, instead of deriving an analytical expression for the spectrum $p^{x}(\lambda;\omega)$, we simply apply the Monte Carlo method based on Eq. (3.7) with randomly generated $\mathbf{J}$ matrices, and $p^{x}(\lambda;\omega)$ can then be estimated by averaging the resulting eigenvalues across many $\mathbf{J}$ realizations. Note that the scalar quantities such as $\langle\phi'\rangle$ and $C^{\phi}(\omega)$ are still computed from the mean-field theory, and this Monte Carlo method remains vastly more efficient than direct simulations of nonlinear networks (Eq. (2.1)).

Our theoretical spectra are confirmed by numerical simulations, which show close matching of the probability density curves and the eigenvalue histograms computed from neural activity (Fig. 2C-F). In particular, the matching is accurate across different dynamical regimes, which is also evidenced by comparing the estimate $g_{\text{eff}}$ from simulations to that from the mean-field theory (Fig. 2B). As the connection strength $g$ increases (while fixing $\sigma$), both $\phi$ and $x$ spectra develop longer tails of large eigenvalues (see also Eq. (4.2) below) corresponding to lower dimension, analogous to the phenomenon seen under linear dynamics [11]. However, this trend will eventually saturate as $g \to \infty$, where the spectra converge to a limiting shape and dimension [4] (see also Section 5). The spectrum of the currents $p^{x}(\lambda;\omega)$ differs from that of the firing rates $p^{\phi}(\lambda;\omega)$ at small eigenvalues with a higher peak density near 0 (Fig. 2D-F, see also the log-log scale insets). In fact, we can use Eq. (3.7) to prove that when $\sigma = 0$ (for all $g$) the left edge of the support of $p^{x}(\lambda;\omega)$ is exactly 0 (Appendix G, Fig. 2F), which is in contrast to the positive left edge of $p^{\phi}(\lambda;\omega)$. These results are consistent with the observation that the dimension of the currents $x$ is lower than that of the firing rates $\phi$, previously noted in [4] (see also Section 5.1 and Appendix I).

Although we do not yet have a closed form expression for the current covariance spectrum $p^{x}(\lambda;\omega)$, we can characterize analytically the large eigenvalues or tail of the spectrum $p^{x}(\lambda;\omega)$ when $g_{\text{eff}} \to 1^{-}$ (its supremum is 1, see Appendix H). This is based on the method from [11] which relates the orders of moments $\mathbb{E}[\lambda^n]$ in terms of $(1-g^2_{\text{eff}})$ and the power-law exponent. We can then use the analytical expressions of the first two moments of $p^{x}(\lambda;\omega)$ (Eq. (D.5) and Eq. (D.7))

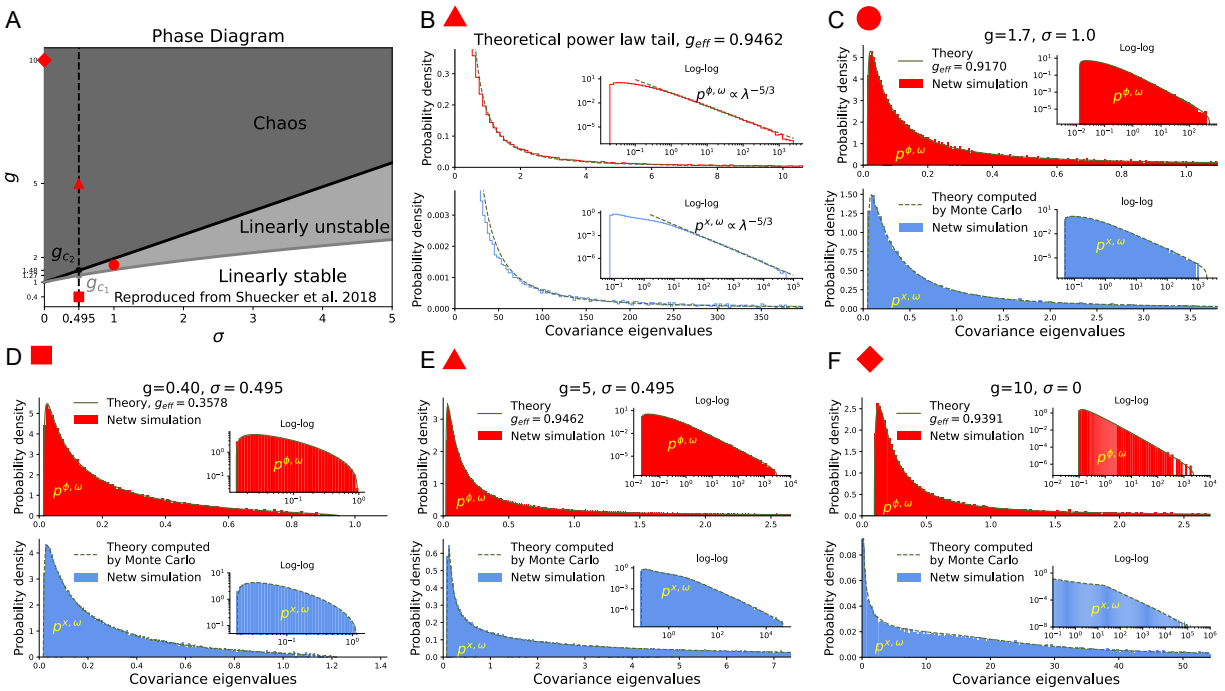


Figure 2: (**A**) Phase diagram of dynamical regimes for the nonlinear randomly connected RNN (Eq. (2.1)), reproduced from [24]. For a fixed input level $\sigma > 0$, there are two critical values $g_{c_1}, g_{c_2}$ of the connection strength $g$ at the regime boundaries, where the larger $g_{c_2}$ separates the chaotic regime. (**B**) Power law approximations (see text) of the tail of covariance spectra from network simulations in the chaotic regime (triangle marker in (A)). (**C-F**) Comparison of the zero-frequency covariance spectra from simulation (a single network and **J**, histograms) and theory (curves, see text) with corrections for finite time samples ([11] and Appendix K) across dynamical regimes including chaos (noise driven and deterministic). For the $x$ theoretical spectra, these are computed using the Monte Carlo method based on Eq. (3.7) (see text). The $(g, \sigma)$ values correspond to the markers in (A), and the network size $N$ is between 3000 and 10000.

to show that (Appendix F),

$$p^{\phi}(\lambda;\omega) \propto \lambda^{-\frac{5}{3}}, \quad p^{x}(\lambda;\omega) \propto \lambda^{-\frac{5}{3}}, \quad \text{when} \quad g_{\text{eff}} \to 1^{-}, \ \ \lambda \to \infty. \tag{4.2}$$

Here we also include the result for $p^{\phi}(\lambda;\omega)$ for comparison, which directly follows from the expression from Eq. (4.1) based on results from [11]. Interestingly, despite clear differences for small eigenvalues (Fig. 2D-F), both spectra $p^{\phi}(\lambda;\omega)$, $p^{x}(\lambda;\omega)$ follow power laws with an identical exponent of $-5/3$, which is the same as that in the linear dynamics [11].

As we show later, for the case with noise input $\sigma > 0$, the effective connection strength $g_{\text{eff}}$ is finitely bounded away from the critical value 1 (Fig. 3D). This is different from the situation when $\sigma = 0$, where $g_{\text{eff}}$ approaches 1 as $g \to 1^{+}$. This means that the power law in Eq. (4.2) is generally an approximation applicable when $g_{\text{eff}}$ is close to 1, and can be accurate even for $g_{\text{eff}} \approx 0.7$ ([11] and Fig. S2). Moreover, such results are important and broadly applicable for describing the covariance spectrum under chaos. This is because $g_{\text{eff}}$ stays close to 1 in the chaotic regime (described later in Section 5.1), so the power law theory (Eq. (4.2)) can be highly accurate (Fig. 2B).

We want to note that our frequency-dependent covariance spectra contain temporal information about the network dynamics [11, 3]. In particular, the zero frequency $\omega = 0$ spectrum describes

correlations over a long time window and, for example, is suitable for analyzing calcium imaging data [11]. Activity and correlation at fast time scales are described by the covariance matrix and spectrum with nonzero $\omega$, where $g_{\text{eff}}$ is replaced by

$$g_{\text{eff}}(\omega) = \frac{g_{\text{eff}}}{\sqrt{1+\omega^2}} = \frac{g\langle\phi'\rangle}{\sqrt{1+\omega^2}}, \tag{4.3}$$

according to Eqs. (3.3) and (3.7) (Fig. S1A). In particular, the power law approximations (Eq. (4.2)) still apply when $g_{\text{eff}}(\omega)$ is close to 1 (Fig. S1A). We can also obtain the time-lagged covariance matrix $\mathbf{C}^a(\tau)$ and the zero time covariance spectrum $p^a(\lambda; \tau = 0)$ (note that the spectrum is only meaningfully defined for $\tau = 0$ where $\mathbf{C}^{\phi,\tau}$ is symmetric positive semidefinite) by numerically taking an entry-wise inverse Fourier transform of the frequency-dependent covariance matrix expressions (Eqs. (3.3) and (3.7), see Appendix J). The zero time lag covariance spectra computed this way match closely with direct nonlinear network simulations (Fig. S1BC).

## 5 Effective connection strength $g_{\text{eff}}$ and transition to chaos

The change of both the dimension and covariance spectrum across dynamical regimes can be described in a unified way by the effective recurrent connection strength $g_{\text{eff}}$ (Eq. (3.2)), which was first introduced in [4] where its importance for determining the dimension was discussed. In particular, the covariance spectrum and dimension for the firing rates $\phi$ (Eqs. (3.1) and (4.1)) all depend on $g_{\text{eff}}$. This can be seen clearly from Eq. (3.3): if we introduce a scaled connectivity matrix $\mathbf{J}_0 = \mathbf{J}/g$, then the matrix $\mathbf{C}^\phi(\omega)$ is, up to a scalar and the shape of its spectrum, dependent only on $g_{\text{eff}}$ and $\mathbf{J}_0$ (and not on $g$). Similar result also holds for the currents $x$ when there is no noise (i.e., the first term in Eq. (3.7) and for dimension, Eq. (D.8) in Appendix D.2). When there is non-zero noise $\sigma > 0$, the covariance matrix and spectrum of $x$ further depend on the relative magnitude between $\sigma^2$, $C^x(\omega)$, and $C^\phi(\omega)$ governed by the mean-field theory Eq. (2.2), which can also be seen in the dimension expression Eq. (3.14).

We can then focus on how $g_{\text{eff}}$ changes with network parameters $g, \sigma$ and across dynamical regimes, especially around the transition to chaos (Fig. 3). First, one can prove that $g_{\text{eff}} = g\langle\phi'\rangle < 1$ for all $g, \sigma$ as long as the dynamics is not a fixed point (Appendix H). For a fixed $\sigma > 0$, in the linear regime (both linearly stable and unstable, Fig. 2A), $g_{\text{eff}}$ increases quickly with $g$ from 0 until the transition to chaos ($g < g_{c_2}$). In the chaotic regime, $g_{\text{eff}}$ stays close to 1 and eventually converges to $1/\sqrt{\pi - 2} \approx 0.9359$ as $g \to \infty$ (Fig. 3B, [4]). This asymmetric behavior of $g_{\text{eff}}$, and consequently for the spectrum and dimension (Fig. 4C,D), on the two sides of the chaos boundary is reminiscent of previous results about memory properties of such networks [28]. The near critical $g_{\text{eff}}$ in the chaotic regime without fine tuning is intriguing. One implication is that we can use a simple power law approximation (Eq. (4.2)) to describe the covariance spectrum. The near critical $g_{\text{eff}}$ may also be related to findings in experimental data, where the fitted $\hat{g}_{\text{eff}}$'s in various brain regions [19] and frequency bands [3] are often close to the critical value of 1.

When fixing $g$, $g_{\text{eff}}$ decreases monotonically with $\sigma$ (Fig. 3C). The existence of nonzero noise also prevents the correlation time $\tau_{1/2}$ of neuron dynamics (defined by $C^a(\tau_{1/2}) = \frac{1}{2}C^a(0)$, $a \in \{x, \phi\}$) from diverging to infinity. Moreover, the maximum of $g_{\text{eff}}$ across $g$ is bounded away from 1 for any fixed $\sigma > 0$ (Fig. 3 and Appendix H), and the only possibility to achieve $g_{\text{eff}} \to 1^-$ is when $\sigma \to 0$ (and $g \to 1$).

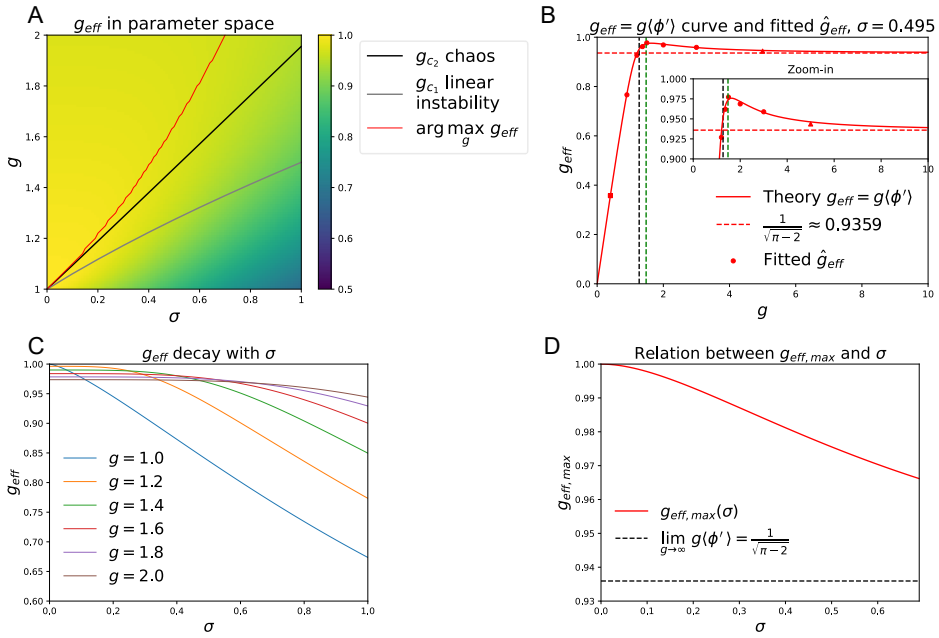


Figure 3: (**A**) The effective connection strength $g_{\text{eff}}$ (color) as a function of $(g, \sigma)$ in the network model Eq. (2.1). The black and gray curves are boundaries for chaos and linear instability regions [24], respectively, and are the same as in Fig. 2A. The red curve shows the location of the maximum of $g_{\text{eff}}$ for each fixed $\sigma$. (**B**). The effective connection strength $g_{\text{eff}} = g\,\langle\phi'\rangle$ (Eq. (3.2)) solved from the mean-field theory (curve) compared with the estimates $\hat{g}_{\text{eff}}$ (dots) obtained by fitting the theoretical covariance spectrum (Eq. (4.1)) to network simulations. (**C**) $g_{\text{eff}}$ as a function of $\sigma$ for different values of $g$. (**D**) The relationship between the maximum of $g_{\text{eff}}$ over $g$ (while fixing $\sigma$, e.g., in (B)) and $\sigma$.

### 5.1 Dimension gap near the transition to chaos

It was noted in [4], that currents and firing rates have different dimensions $D^{\phi,\tau} > D^{x,\tau}$ (Fig. 4A, $D^{a,\tau}$ is the zero time lag dimension for $\mathbf{C}^a(\tau = 0)$), and the *dimension gap*

$$\Delta D := D^{\phi} - D^{x} \tag{5.1}$$

decreases to 0 when $g \to 1^+$ approaching its critical value for chaos ([4], Fig. 4A, bottom). However, in this deterministic model considered in [4], one is limited to the range of $g > 1$ (the network remains at a fixed point for $g < 1$). In contrast, our noise-driven model Eq. (2.1) allows us to examine the full picture of the dimension gap during the transition from linear to chaotic regimes (Fig. 2A). It is then natural to ask for this general noise-driven system: Does the dimension gap still vanish at the transition to chaos? Are the rate and current dimensions exactly equal within the linear regimes?

We give conclusive answers to these questions using the theoretical expressions for the dimension (Eqs. (3.1) and (3.14)), which are also supported by extensive direct simulations of the network. We find that the dimension gap $\Delta D$ is always positive (see Appendix I for a proof for the frequency-dependent dimensions) and has a non-monotonic dependence on $g$ for $\sigma > 0$. It has a local maximum in the linear stable regime, and a local minimum before increasing with $g$ in the chaotic regime (Fig. 4B,C). The nontrivial local minimum of $\Delta D$ is analogous to the vanishing of $\Delta D$ at $g \to 1^+$ in the $\sigma = 0$ case, but the local minimum is located near but not coinciding with the chaos boundary (Fig. S3).

The above phenomena of dimension gap hold for both zero time lag (Fig. 4A,C) and frequency-dependent and dimensions (Fig. 4B,D). For the zero time lag dimensions, $D^{\phi,\tau}$ and $D^{x,\tau}$ converge to their theoretical asymptotic values of 0.126 and 0.0602, respectively (Appendix J, [4]). These asymptotic values are identical with or without noise input (Fig. 4A,C, see Appendix J) and match with previous results on the noiseless case [4]. For the frequency-dependent dimensions, their asymptotic values can be obtained from Eqs. (3.1) and (3.14) using the limit $g_{\text{eff}} = g\langle\phi'\rangle \to 1/\sqrt{\pi-2}$ [4, 1],

$$\lim_{g\to\infty} D^{\phi}(\omega) = \left[\frac{(1+\omega^2)(\pi-2)-1}{(1+\omega^2)(\pi-2)}\right]^2, \quad \lim_{g\to\infty} D^{x}(\omega) = \frac{\left[(1+\omega^2)(\pi-2)-1\right]^2}{2(1+\omega^2)^2(\pi-2)^2-1}. \tag{5.2}$$

Again there is no dependence on the magnitude of noise input $\sigma$ (Fig. 4B,D). At zero frequency $\omega = 0$, the limiting dimensions are approximately 0.0154 and 0.0125, respectively.

We wanted to note that since the dimension gap, and even the dimensions themselves, are very small in magnitude around the chaotic regime (see the y-axis scale in Fig. 4C,D, insets), it would be difficult to determine the above properties of $\Delta D$ "by eye" using only simulations of the network. Therefore, the accurate and asymptotically exact ($N \to \infty$) theory (Eqs. (3.1) and (3.14)) is crucial for reaching our conclusions delineating the relationship between dimension gap and transition to chaos.

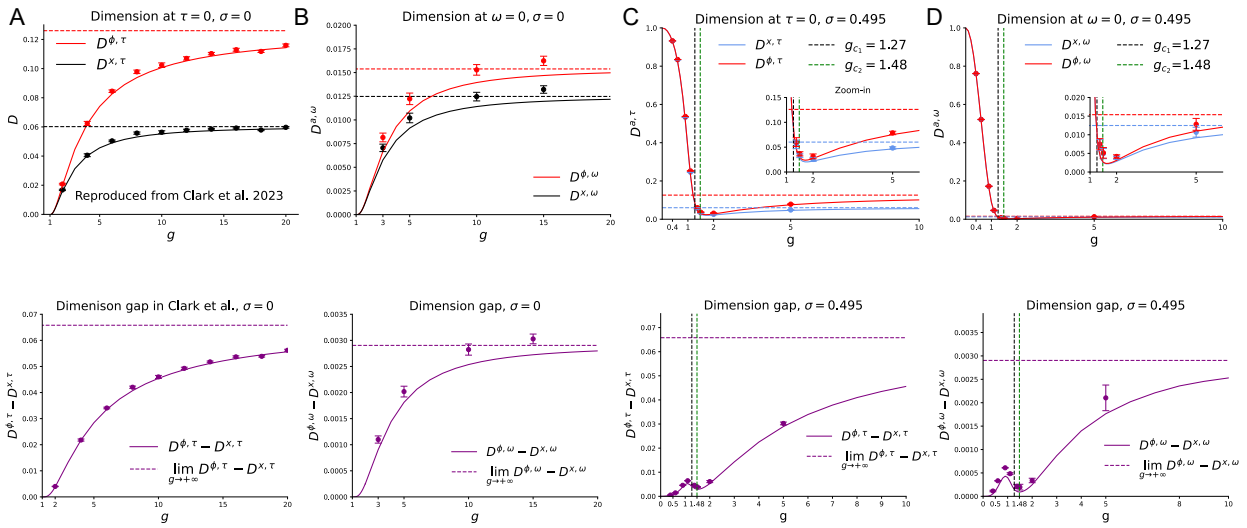


Figure 4: (**A**) Zero time lag dimensions $D^{a,\tau}(\tau = 0)$, $a \in \{x, \phi\}$ for currents and firing rates in the deterministic case with $\sigma = 0$ (reproduced from [4], top) and the dimension gap $\Delta D^{\tau}$ (bottom). The solid curves are theory ([4], Appendix J) and dots are averages from simulating Eq. (2.1) ($N = 4000$ with 5 realizations of $\mathbf{J}$ and error bars are standard errors across network realizations). Dashed lines are the asymptotic values when $g \to \infty$. (**B**) Same as (A), but for the zero-frequency dimensions $D^{a}(\omega = 0)$ based on the frequency-dependent theory Eqs. (3.1) and (3.14) (see also Fig. S4 for discussion on deviations with simulations). (**C**) Same as (A), but with noise input $\sigma = 0.495$. (**D**) Same as (C), but for zero-frequency dimensions.

# 6 Discussion

In this paper, we derived a theory for the covariance spectrum in randomly connected recurrent networks with nonlinear neuronal dynamics. The results are exact in the large network limit and are valid across various dynamical regimes, including chaos. These results on the covariance spectrum provide a precise description and important insights into neural population dynamics, particularly regarding its shape beyond dimensionality. Since our results on the covariance matrix and spectrum are expressed in a frequency-dependent form (Eqs. (3.3) and (3.7)), they describe describe neural activity in each frequency band which can be an informative description [3]. The frequency dependent covariance also contains information about the temporal dynamics. Moreover, time-domain quantities, such as the time-lagged covariance spectrum, can be obtained through an inverse Fourier transform (Fig. S1BC).

The key to deriving these results is the firing rate covariance matrix ansatz and its corollary (Eqs. (3.3) and (3.7)), which provide a concrete and explicit link between neuronal nonlinear dynamics and recurrent network connectivity in the covariance matrices. Our results are confirmed by extensive numerical simulations (Figs. 1 and 2). These findings significantly extend previous theory on the covariance spectrum derived under linear dynamics [11] and therefore provide further theoretical support for applying the covariance spectrum analysis to data. In particular, our results offer insights for interpreting the fitted recurrent connection strength $\hat{g}$ as an effective parameter $g_{\text{eff}}$, reflecting both anatomical connection weights and the nonlinear neuronal dynamics.

Our theory on the covariance matrix and spectrum highlights the unified role of the effective recurrent connection strength $g_{\text{eff}}$, whose importance now extends beyond determining the dimension [4]. This suggests a simple, conceptual framework for understanding nonlinear network dynamics: while $g_{\text{eff}}$ can be derived from classical mean-field theory focusing on a single neuron's dynamics [24], the effects of the recurrent connections are then summarized in our closed-form covariance matrix expressions (Eqs. (3.3) and (3.7)), which contain interaction terms of all orders, such as $\mathbf{J}\mathbf{J}^T$, $\mathbf{J}^2(\mathbf{J}^T)^2$, and $\mathbf{J}\mathbf{J}^T\mathbf{J}\mathbf{J}^T\mathbf{J}\mathbf{J}^T$.

We studied how $g_{\text{eff}}$ changes across different dynamical regimes and through the transition to chaos (Fig. 2B, Fig. 3B). Importantly, this revealed asymmetric trends on the two sides of the edge of chaos [28]: a rapid increase in the linear regimes, while $g_{\text{eff}}$ remains consistently close to the critical value of 1 in the chaotic regime without fine-tuning. This finding is potentially related to the observation that fitting experimental neural activity data often results in near-critical $g_{\text{eff}}$ values [19, 3]. Furthermore, we characterized a more general version of the phenomenon of a diminishing dimension gap near the transition to chaos (Fig. 4), previously noted in [4], thus revealing a full picture across various dynamical regimes.

This work serves as a basis for further exploring the complex geometry of population dynamics in nonlinear systems, particularly in the chaotic regime, and many interesting questions remain open for future investigation. For example, it would be interesting to explore more general types of recurrent network connectivity, such as those containing motifs [31, 12], spatially dependent connectivity [14] and with heterogeneous degrees [13]. On the technical side, it is important to develop methods that directly derive the covariance matrix ansatz (Eq. (3.3)), for example, by proving the independence property of the effective noise $\zeta$ (Eq. (3.8)).


# Acknowledgment

This work was partly supported by a ECS grant 26303921 from the Research Grants Council of Hong Kong.

## References


[1] A.Crisanti and H.Sompolinsky (2018). Path integral approach to random neural network. *Phys Rev E*, 98:188104.

[2] Ahrens, M. B., Li, J. M., Orger, M. B., Robson, D. N., Schier, A. F., Engert, F., and Portugues, R. (2012). Brain-wide neuronal dynamics during motor adaptation in zebrafish. *Nature*, 485:471–477.

[3] Calvo, R., Martorell, C., Morales, G. B., Di Santo, S., and Muñoz, M. A. (2024). Frequency-dependent covariance reveals critical spatiotemporal patterns of synchronized activity in the human brain. *Phys. Rev. Lett.*, 133:208401.

[4] Clark, D. G., Abbott, L. F., and Litwin-Kumar, A. (2023). Dimension of activity in random neural networks. *Physical Review Letters*, 131.

[5] Dahmen, D., Recanatesi, S., Ocker, G. K., Jia, X., Helias, M., and Shea-Brown, E. (2023). Strong coupling and local control of dimensionality across brain areas. *bioRxiv*.

[6] Fusi, S., Miller, E. K., and Rigotti, M. (2016). Why neurons mix: High dimensionality for higher cognition. *Current Opinion in Neurobiology*, 37:66–74.

[7] Gallego, J. A., Perich, M. G., Miller, L. E., and Solla, S. A. (2017). Neural Manifolds for the Control of Movement. *Neuron*, 94(5):978–984.

[8] Gardiner, C. (2009). *Handbook of Stochastic Methods for Physics, Chemistry and the Natural Sciences*. Springer-Verlag, Berlin.

[9] Gozel, O. and Doiron, B. (2024). Between-area communication through the lens of within-area neuronal dynamics. *Science Advances*, 10(42):eadl6120.

[10] Hu, Y., Brunton, S. L., Cain, N., Mihalas, S., Kutz, J. N., and Shea-brown, E. (2018). Feedback through graph motifs relates structure and function in complex networks. *Physical Review E*, 062312:1–25.

[11] Hu, Y. and Sompolinsky, H. (2022). The spectrum of covariance matrices of randomly connected recurrent neuronal networks with linear dynamics. *PLoS Computational Biology*, 18.

[12] Hu, Y., Trousdale, J., Josić, K., and Shea-Brown, E. (2013). Motif statistics and spike correlations in neuronal networks. *Journal of Statistical Mechanics: Theory and Experiment*, 2013(03):P03012.

[13] Hu, Y., Trousdale, J., Josić, K., and Shea-Brown, E. (2014). Local paths to global coherence: Cutting networks down to size. *Physical Review E - Statistical, Nonlinear, and Soft Matter Physics*, 89(3):1–16.

[14] Huang, C., Ruff, D. A., Pyle, R., Rosenbaum, R., Cohen, M. R., and Doiron, B. (2019). Circuit models of low-dimensional shared variability in cortical networks. *Neuron*, 101(2):337–348.e4.

[15] Jun, J., Steinmetz, N., Siegle, J., Denman, D., Bauza, M., Barbarits, B., Lee, A., Anastassiou, C., Andrei, A., Aydin, C., Barbic, M., Blanche, T., Bonin, V., Couto, J., Dutta, B., Gratiy, S., Gutnisky, D., Häusser, M., Karsh, B., and Harris, T. (2017). Fully integrated silicon probes for high-density recording of neural activity. *Nature*, 551:232–236.

[16] Kadmon, J. and Sompolinsky, H. (2015). Transition to chaos in random neuronal networks. *Physical Review X*, 5(4):1–28.

[17] Litwin-Kumar, A., Harris, K. D., Axel, R., Sompolinsky, H., and Abbott, L. F. (2017). Optimal Degrees of Synaptic Connectivity. *Neuron*, 93(5):1153–1164.e7.

[18] Mastrogiuseppe, F. and Ostojic, S. (2018). Linking connectivity, dynamics, and computations in low-rank recurrent neural networks. *Neuron*, 99(3):609–623.e29.

[19] Morales, G. B., di Santo, S., and Muñoz, M. A. (2023). Quasiuniversal scaling in mouse-brain neuronal activity stems from edge-of-instability critical dynamics. *Proceedings of the National Academy of Sciences*, 120(9):e2208998120.

[20] Novikov, E. A. (1965). Functionals and the random-force method in turbulence theory. *Soviet Journal of Experimental and Theoretical Physics*, 20(5):1290–1294.

[21] Price, R. (1958). A useful theorem for nonlinear devices having gaussian inputs. *IRE Transactions on Information Theory*, 4(2):69–72.

[22] Rajan, K., Abbott, L. F., and Sompolinsky, H. (2011). *The Dynamic Brain: An Exploration of Neuronal Variability and Its Functional Significance*, chapter Interactions between Intrinsic and Stimulus-Evoked Activity in Recurrent Neural Networks, pages 65–82. Oxford University Press.

[23] Recanatesi, S., Ocker, G. K., Buice, M. A., and Shea-Brown, E. (2019). Dimensionality in recurrent spiking networks: Global trends in activity and local origins in connectivity. *PLoS Computational Biology*, 15(7):1–29.

[24] Schuecker, J., Goedeke, S., and Helias, M. (2018). Optimal sequence memory in driven random networks. *Physical Review X*, 8(4):041029.

[25] Semedo, J. D., Zandvakili, A., Machens, C. K., Yu, B. M., and Kohn, A. (2019). Cortical Areas Interact through a Communication Subspace. *Neuron*, 102(1):249–259.e4.

[26] Sompolinsky, H., Crisanti, a., and Sommers, H. J. (1988). Chaos in random networks. *Phys. Rev. Lett.*, 61(3):259–262.

[27] Stringer, C., Pachitariu, M., Steinmetz, N., Reddy, C. B., Carandini, M., and Harris, K. D. (2019). Spontaneous behaviors drive multidimensional, brainwide activity. *Science*, 364(6437):eaav7893.

[28] Toyoizumi, T. and Abbott, L. F. (2011). Beyond the edge of chaos: Amplification and temporal integration by recurrent networks in the chaotic regime. *Phys. Rev. E*, 84:051908.

[29] Trousdale, J., Hu, Y., Shea-Brown, E., and Josić, K. (2012). Impact of network structure and cellular response on spike time correlations. *PLoS Comput Biol*, 8(3):e1002408.

[30] Wang, Z., Mai, W., Chai, Y., Qi, K., Ren, H., Shen, C., Zhang, S., Tan, G., Hu, Y., and Wen, Q. (2025). The geometry and dimensionality of brain-wide activity. *eLife*.

[31] Zhao, L., Beverlin, B., Netoff, T., and Nykamp, D. Q. (2011). Synchronization from second order network connectivity statistics. *Front Comput Neurosci*, 5:1–16.

# Appendix

## A Supplementary figures

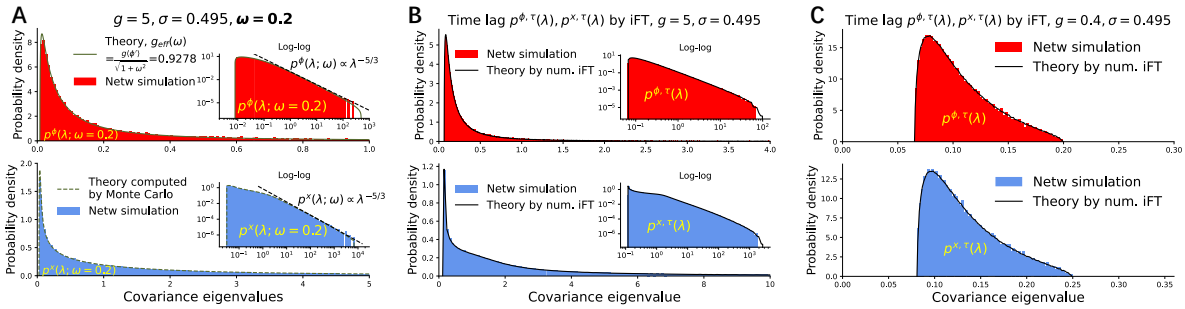


Figure S1: (**A**) Nonzero-frequency covariance spectrum $p^{\phi}(\lambda;\omega = 0.2)$ and $p^{x}(\lambda;\omega = 0.2)$ of a network at $g = 5$, $\sigma = 0.495$ (same as Fig. 2E in the chaotic regime). The frequency-dependent effective connection parameter is $g_{\text{eff}}(\omega) = g\langle\phi'\rangle/\sqrt{1+\omega^2}$ (Eq. (4.3)). (**B**) Zero time lag covariance spectrum $p^{\phi,\tau}(\lambda)$ and $p^{x,\tau}(\lambda)$ of a network at $g = 5$, $\sigma = 0.495$ (same as (A) and Fig. 2E). The theory curve is computed by an entry-wise inverse Fourier transform of the covariance matrices (Eq. (3.3)) and averaged over 10 realizations of $\mathbf{J}$ with $N = 10000$ (see Appendix J). (**C**) Same as (B), but for a network in the linearly stable regime (Fig. 2A, $g = 0.4$, $\sigma = 0.495$, same as Fig. 2D).

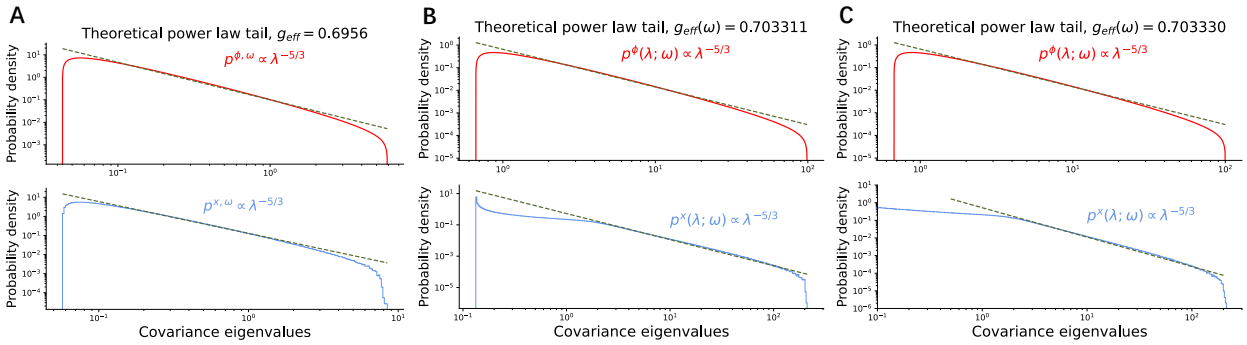


Figure S2: Power law approximations to the theoretical covariance spectra $p^{\phi}(\lambda;\omega)$ and $p^{x}(\lambda;\omega)$ (Eq. (4.2)) at $g_{\text{eff}}(\omega) = g\langle\phi'\rangle/\sqrt{1+\omega^2} \approx 0.7$. Note that $g_{\text{eff}}(\omega)$ depends on $g$, $\sigma$, and the frequency $\omega$. Therefore, we show here three different combinations of parameters corresponding to $g_{\text{eff}}(\omega) \approx 0.7$. In all cases, the tail of the theoretical spectra (Section 4) are well approximated by the power law given in Eq. (4.2). (**A**) $g = 0.8$, $\sigma = 0.495$, $\omega = 0$, and $g_{\text{eff}} = 0.6956$. (**B**) $g = 5$, $\sigma = 0.495$, $\omega = 0.9$, and $g_{\text{eff}}(\omega) = 0.7033$. (**C**) $g = 5$, $\sigma = 0$, $\omega = 0.9$, and $g_{\text{eff}}(\omega) = 0.7033$.

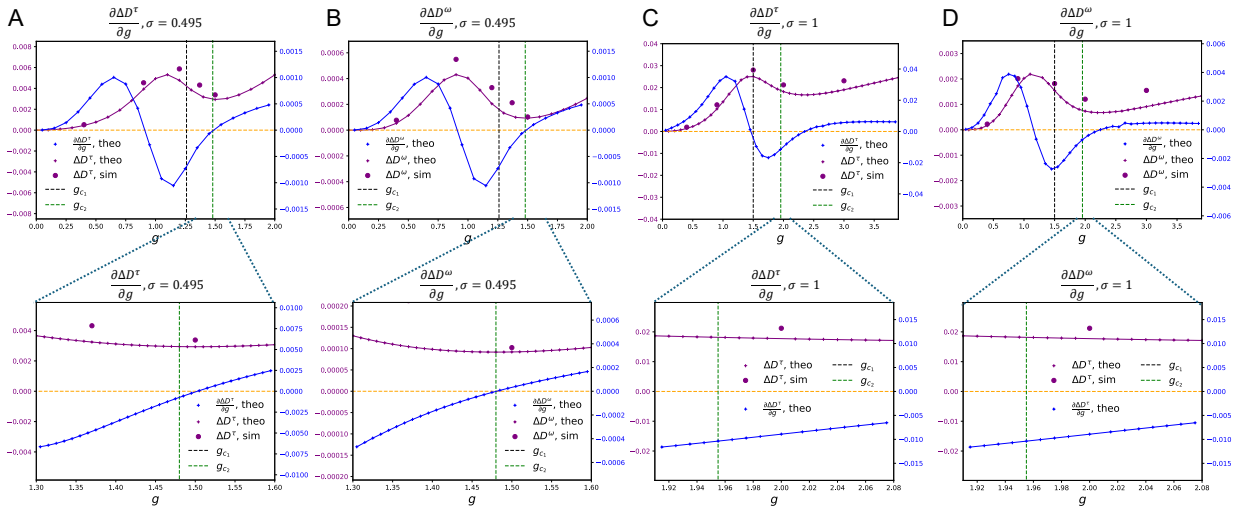


Figure S3: (**A**) The theoretical zero time lag dimension gap $\Delta D^\tau = D^{\phi,\tau} - D^{x,\tau}$ (purple cross and line, Eq. (5.1)) and its derivative (blue cross and line) for $\sigma = 0.495$. Direct network simulations (large purple dots) confirm the trend predicted by the theory. The bottom panel shows a zoom-in near the transition to chaos ($g_{c_2} = 1.48$). (**B**) Same as (A), but for the zero-frequency dimension gap $\Delta D^\omega = D^{\phi,\omega} - D^{x,\omega}$. Note the closeness of $\partial \Delta D^\omega / \partial g = 0$ and $g_{c_2}$ is a coincidence (see (D) for a different $\sigma$). (**C,D**) Same as (A,B), but for $\sigma = 1$. It is clear that the local minimum of the dimension gap $\Delta D$ lies within the chaotic regime.

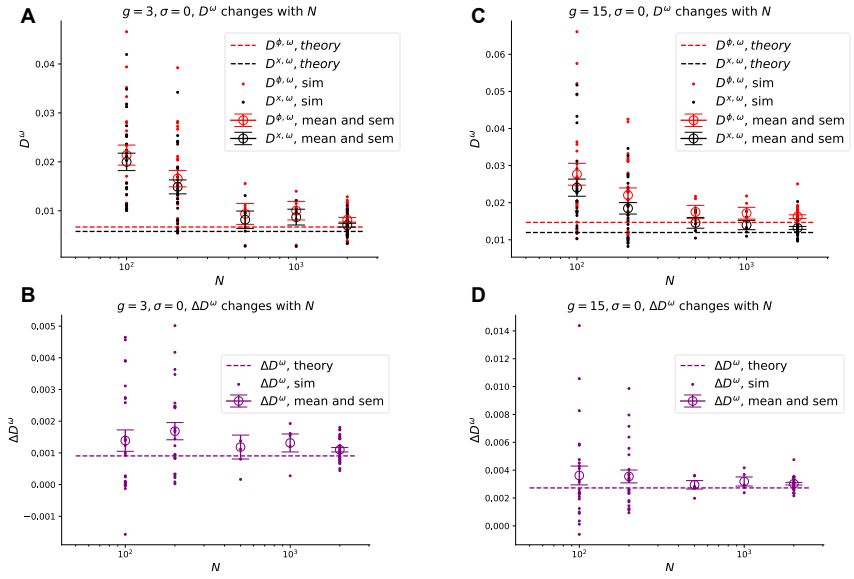


Figure S4: The zero-frequency dimensions (**A,C**) and the dimension gap (**B,D**) converge to the mean-field theory values as $N \to \infty$. The dots are computed from network simulations (Eq. (L.1)), and circles and error bars denote the mean and standard error of the mean (SEM) across network realizations, respectively. The dashed lines correspond to theoretical values (Eqs. (3.1) and (3.14)). The networks are deterministic with $\sigma = 0$ corresponding to Fig. 4B, and the parameter values of $g = 3$ (A,B) and $g = 15$ (C,D) are representative of the plotted range of $g$. These figures therefore support that the deviations seen in Fig. 4B are likely finite-size effects.

## B Four-point function $\psi^a(\omega_1, \omega_2)$ and dimension when $\sigma \geq 0$ via cavity method

In this section, we will derive the frequency-dependent four-point function $\psi^\phi(\boldsymbol{\omega})$ and $\psi^x(\boldsymbol{\omega})$ with $\boldsymbol{\omega} = (\omega_1, \omega_2)$ based on two-site cavity method in [4], which dealt with the deterministic case of $\sigma = 0$. Here we extend the four-point function results to the case with noise input $\sigma \geq 0$. While the majority of steps are the same as in [4] and we include here for completeness, some steps around Eq. (B.4) are different from the $\sigma = 0$ case (specifically Eq. B3 in [4]).

The cavity method will introduce extra auxiliary neurons, or cavity neurons, then compute the perturbation effects due to these cavity neurons. The method is based on the notion that the statistics of cavity neurons are equivalent to any other, regular neurons in network. We introduce two *cavity neurons* with indices $0, 0'$, with connectivity $J_{\mu i}$, $J_{i\mu} \sim \mathcal{N}\left(0, g^2/N\right)$ for $\mu \in \{0, 0'\}$, $i \in \{1, \cdots, N\}$ (same as the rest of network). We refer the rest of neurons with index $i, j \in \{1, \cdots, N\}$ as the *reservoir neurons*. The activities of the cavity neurons is driven by three components: (i) input from the reservoir, (ii) input from mutual and self-connections, and (iii) from external noise input. We have

$$\begin{cases} (1+\partial_t) x_i^{\text{free}}(t) = \sum_{j=1}^{N} J_{ij} \phi_j^{\text{free}}(t) + \xi_i(t) = \eta_i(t) + \xi_i(t), \\ (1+\partial_t) x_\mu^{\text{free}}(t) = \sum_{i=1}^{N} J_{\mu i} \phi_i^{\text{free}}(t) + \xi_\mu(t) = \eta_\mu(t) + \xi_\mu(t). \end{cases} \tag{B.1}$$

Here $\phi_\mu^{\text{free}}(t) = \phi(x_\mu^{\text{free}}(t))$. As in the main text, we denote $a \in \{\phi, x\}$ for simplicity and reduces parallel equations. When $a(t)$ is labeled with a superscript "free", it mean there is no feedback from cavity neuron to reservoir, i.e., $J_{i\mu} = 0$, and no mutual connection $J_{\mu\nu} = 0$. This means, the input field to cavity unit $\eta_\mu(t) = \sum_{i=1}^{N} J_{\mu i} \phi_i^{\text{free}}(t)$ does not correlate to $\xi_\nu(t)$ at all for $\mu, \nu \in \{0, 0'\}$, i.e., $\langle \eta_\mu(t) \xi_\nu(t+\tau) \rangle = 0$. This is different from within-reservoir correlation $\langle \eta_i(t) \xi_j(t+\tau) \rangle \neq 0$, $i, j \in \{1, \cdots, N\}$. Firing rate of neuron $i$ is perturbed by $\delta\phi_i(t) = \int_0^t \sum_{j=1}^{N} \sum_{\mu \in \{0,0'\}} S_{ij}^{\phi}(t, t') J_{j\mu} \phi_\mu^{\text{free}}(t') dt'$. Note that $(\eta_0(t), \eta_{0'}(t'))$ are jointly Gaussian distributed [4]. These distribution results are used to justify applying the Stein's lemma around Eq. (B.4). We expand the cavity neuron activities (both $\phi_\mu$ and $x_\mu$) perturbed by feedback, mutual, and self-connections up to leading orders in $1/\sqrt{N}$,

$$a_\mu(t) = a_\mu^{\text{free}}(t) + \frac{1}{\sqrt{N}} \int^t dt' S_{\mu\mu}^a(t, t') \int^{t'} dt'' \sum_{\nu \in \{0,0'\}} F_{\mu\nu}(t', t'') \phi_\nu^{\text{free}}(t'') + O\left(\frac{1}{N}\right). \tag{B.2}$$

Here $S_{ij}^a(t, t')$ is linear response function for $a \in \{x, \phi\}$ and we write $S_{ij}^a(\tau) = \left\langle S_{ij}^a(t, t-\tau) \right\rangle$. Similarly, $F_{\mu\nu}(t, t')$ describes the overall influence of $\nu$ on $\mu$, and $F_{\mu\nu}(\tau) = \langle F_{\mu\nu}(t, t-\tau) \rangle$. Following the definitions in [4] with the modification of $\tilde{\eta}_\mu = \eta_\mu + \xi_\mu$,

$$S_{ij}^a(t, t') = \left\langle \delta a_i(t) / \delta \tilde{\eta}_j(t') \right\rangle,$$

$$F_{\mu\nu}(t, t') = \sqrt{N} \left[ \sum_{i,j=1}^{N} J_{\mu i} S_{ij}^{\phi}\left(t, t'\right) J_{j\nu} + J_{\mu\nu} \delta(t - t') \right].$$

Next, we compute $\langle a_0(t) a_{0'}(t+\tau) \rangle_t$, the two-point function, using Eq. (B.2) and keep terms up

to $O\left(1/\sqrt{N}\right)$. This is because those higher order terms vanish in later derivations,

$$\begin{aligned}
&\langle a_0(t)a_{0'}(t+\tau)\rangle_t = \left\langle a_0^{\text{free}}(t)a_{0'}^{\text{free}}(t+\tau)\right\rangle_t \\
&+\frac{1}{\sqrt{N}}\left\langle a_0^{\text{free}}(t)\int^t dt' S^a_{0'0'}(t+\tau,t')\int^{t'} dt'' \sum_{\nu\in\{0,0'\}} F_{0'\nu}(t',t'')\phi_\nu^{\text{free}}(t'')\right\rangle_t \\
&+\frac{1}{\sqrt{N}}\left\langle \int^t dt' S^a_{00}(t,t')\int^{t'} dt'' \sum_{\nu\in\{0,0'\}} F_{0\nu}(t',t'')\phi_\nu^{\text{free}}(t'')a_{0'}^{\text{free}}(t+\tau)\right\rangle_t .
\end{aligned} \tag{B.3}$$

For the term of the two point function of unperturbed $a^{\text{free}}$, we expand it in terms of $C^\eta_{00'}$ and use the Price's theorem [21],

$$\begin{aligned}
\left\langle a_0^{\text{free}}(t)a_{0'}^{\text{free}}(t+\tau)\right\rangle_t &= \int ds\int ds' \left\langle \frac{\delta a_0^{\text{free}}(t)}{\delta\tilde{\eta}_0(s)}\frac{\delta a_{0'}^{\text{free}}(t+\tau)}{\delta\tilde{\eta}_{0'}(\tau-s')}\right\rangle_t C^{\tilde{\eta}}_{00'}(s'-s) \\
&= \int ds\int ds' S^a(-s)S^a(\tau-s')C^\eta_{00'}(s'-s).
\end{aligned} \tag{B.4}$$

Note that in the steps of deriving the above, several terms unique due to the case with noise input $\sigma>0$ appear, but they turn out to be all zero: $C^\xi_{00'}(s'-s)=C^{\eta\xi}_{00'}(s'-s)=C^{\eta\xi}_{0'0}(s'-s)=0$. This is because in Eq. (B.1) there is no feedback connections from cavity neurons to the reservoir and thus $\xi_\mu$ have no effect on reservoir $x_i$. Here $C^\eta_{00'}(s'-s)$ describes the correlation between recurrent input $\eta$ of cavity neurons $0,0'$. We can find the Fourier transform of $C^{a^{\text{free}}}_{00'}(\tau)=\left\langle a_0^{\text{free}}(t)a_{0'}^{\text{free}}(t+\tau)\right\rangle_t$ as $C^{a^{\text{free}}}_{00'}(\omega)=|S^a(\omega)|^2C^\eta_{00'}(\omega)$. Keeping only $O(1/\sqrt{N})$ terms, the Fourier transform of Eq. (B.3) is then,

$$C^a_{00'}(\omega)=|S^a(\omega)|^2C^\eta_{00'}(\omega)+\frac{1}{\sqrt{N}}\left[(F_{00'}(\omega)S^a(\omega))^*+F_{0'0}(\omega)S^a(\omega)\right]C^{\phi a}(\omega). \tag{B.5}$$

To proceed, note that $C^{\phi x}(\omega)=\langle\phi'\rangle C^x(\omega)=C^{\phi x}(-\omega)$ using the Stein's lemma and $C^x(\omega)$ being an even function. Using the definition of $\psi^a(\boldsymbol{\omega})$ and plugging in Eq. (B.5),

$$\begin{aligned}
&\frac{1}{N}\psi^a(\boldsymbol{\omega})=\langle C^a_{00'}(\omega_1)C^a_{00'}(\omega_2)\rangle_{\mathbf{J}}=\left\langle|S^a(\omega_1)S^a(\omega_2)|^2C^\eta_{00'}(\omega_1)C^\eta_{00'}(\omega_2)\right\rangle_{\mathbf{J}} \\
&+\frac{1}{\sqrt{N}}\left\langle|S^a(\omega_1)|^2[(F_{00'}(\omega_2)S^a(\omega_2))^*+(F_{0'0}(\omega_2)S^a(\omega_2))]C^\eta_{00'}(\omega_1)C^{\phi a}(\omega_2)\right\rangle_{\mathbf{J}} \\
&+\frac{1}{\sqrt{N}}\left\langle|S^a(\omega_2)|^2[(F_{00'}(\omega_1)S^a(\omega_1))^*+(F_{0'0}(\omega_1)S^a(\omega_1))]C^\eta_{00'}(\omega_2)C^{\phi a}(\omega_1)\right\rangle_{\mathbf{J}} \\
&+\frac{1}{N}\langle F^*_{00'}(\omega_1)F_{0'0}(\omega_2)(S^a(\omega_1))^*S^a(\omega_2)+(F_{00'}(\omega_1)F_{00'}(\omega_2)S^a(\omega_1)S^a(\omega_2))^* \\
&+F_{0'0}(\omega_1)F_{0'0}(\omega_2)S^a(\omega_1)S^a(\omega_2)+F_{0'0}(\omega_1)F^*_{00'}(\omega_2)S^a(\omega_1)(S^a(\omega_2))^*\rangle_{\mathbf{J}}\,C^{\phi a}(\omega_1)C^{\phi a}(\omega_2).
\end{aligned} \tag{B.6}$$

For $\mathbf{J}$ with zero-mean i.i.d. entries, only selective terms in the above are nonzero as $N\to\infty$: $\left\langle C^\eta_{00'}(\omega_1)C^\eta_{00'}(\omega_2)\right\rangle_{\mathbf{J}}$, $\langle F_{00'}(\omega_1)F_{00'}(\omega_2)\rangle_{\mathbf{J}}$, and $\langle F_{0'0}(\omega_1)F_{0'0}(\omega_2)\rangle_{\mathbf{J}}$. Hence the above equation simplifies to,

$$\begin{aligned}
\psi^a(\boldsymbol{\omega}) &= N|S^a(\omega_1)S^a(\omega_2)|^2\left\langle C^\eta_{00'}(\omega_1)C^\eta_{00'}(\omega_2)\right\rangle_{\mathbf{J}} \\
&+\langle F_{00'}(\omega_1)F_{00'}(\omega_2)\rangle_{\mathbf{J}}\,S^a(\omega_1)S^a(\omega_2)C^{\phi a}(\omega_1)C^{\phi a}(\omega_2) \\
&+\left(\langle F_{00'}(\omega_1)F_{00'}(\omega_2)\rangle_{\mathbf{J}}\,S^a(\omega_1)S^a(\omega_2)\right)^*C^{\phi a}(\omega_1)C^{\phi a}(\omega_2).
\end{aligned} \tag{B.7}$$

To proceed with mean-field arguments, we have

$$\begin{aligned}\left\langle C^{\eta}_{00'}(\omega_1)C^{\eta}_{00'}(\omega_2)\right\rangle_{\mathbf{J}} &= \left\langle \sum_{i,j=1}^{N} J^2_{0i}J^2_{0'j}C^{\phi}_{ij}(\omega_1)C^{\phi}_{ij}(\omega_2) + \sum_{k\neq i,l\neq j}^{N} J_{0i}J_{0k}J_{0'j}J_{0'l}C^{\phi}_{ij}(\omega_1)C^{\phi}_{kl}(\omega_2)\right\rangle_{\mathbf{J}} \\ &= \frac{g^4}{N}C^{\phi}(\omega_1)C^{\phi}(\omega_2) + \frac{g^4}{N}\psi^{\phi}(\boldsymbol{\omega}) + 0,\end{aligned}$$

and similarly,

$$\begin{aligned}\left\langle F_{00'}(\omega_1)F_{00'}(\omega_2)\right\rangle_{\mathbf{J}} &= g^4 S^{\phi}(\omega_1)S^{\phi}(\omega_2) + g^4 N\left\langle S^{\phi}_{00'}(\omega_1)S^{\phi}_{00'}(\omega_2)\right\rangle_{\mathbf{J}} + g^2 \\ &= g^4 S^{\phi}(\omega_1)S^{\phi}(\omega_2) + g^4\left[S^{\phi}(\omega_1)S^{\phi}(\omega_2)\right]^2\left\langle F_{00'}(\omega_1)F_{00'}(\omega_2)\right\rangle_{\mathbf{J}} + g^2.\end{aligned} \tag{B.8}$$

Note that $S^{\phi}_{00'}(\omega) = N^{-1/2}S^{\phi}(\omega)^2 F_{00'}(\omega)$ [4]. We can therefore solve $\left\langle F_{00'}(\omega_1)F_{00'}(\omega_2)\right\rangle_{\mathbf{J}}$ from the last equation,

$$\left\langle F_{00'}(\omega_1)F_{00'}(\omega_2)\right\rangle_{\mathbf{J}} = \frac{g^2}{1 - g^2 S^{\phi}(\omega_1)S^{\phi}(\omega_2)}. \tag{B.9}$$

Using the Furutsu-Novikov theorem [20], one can show that $S^{\phi}(\omega) = C^{\eta\phi}(\omega)/C^{\eta}(\omega)$ [4]. Then applying the Stein's lemma, $C^{\eta\phi}(\omega) = \langle\phi'\rangle\, C^{\eta x}(\omega)$, results in

$$S^{\phi}(\omega) = \langle\phi'\rangle\, S^{x}(\omega) = \frac{\langle\phi'\rangle}{1 + i\omega}. \tag{B.10}$$

Finally, plugging Eqs. (B.8) and (B.10) into Eq. (B.7), and using $C^{\phi x}(\omega) = \langle\phi'\rangle\, C^{x}(\omega)$ (Stein's lemma), we obtain the frequency-dependent four-point functions valid for $\sigma \geq 0$,

$$\psi^{\phi}(\boldsymbol{\omega}) = \left[\frac{|X(\boldsymbol{\omega})|^2}{\left|X(\boldsymbol{\omega}) - g^2\langle\phi'\rangle^2\right|^2} - 1\right] C^{\phi}(\omega_1)C^{\phi}(\omega_2), \quad \text{where } X(\omega) = (1 + i\omega_1)(1 + i\omega_2), \tag{B.11}$$

$$\psi^{x}(\boldsymbol{\omega}) = \frac{g^4}{\left|X(\boldsymbol{\omega}) - g^2\langle\phi'\rangle^2\right|^2} C^{\phi}(\omega_1)C^{\phi}(\omega_2) + \left[\frac{|X(\boldsymbol{\omega})|^2 - g^4\langle\phi'\rangle^4}{\left|X(\boldsymbol{\omega}) - g^2\langle\phi'\rangle^2\right|^2} - 1\right] C^{x}(\omega_1)C^{x}(\omega_2). \tag{B.12}$$

The second moment of these frequency-dependent covariance matrices can then be obtained by setting $\omega_1 = -\omega_2 = \omega$, and write $\psi^a(\omega) := \psi^a(\omega, -\omega)$,

$$\begin{aligned}\varphi_2\left[\mathbf{C}^{\phi}(\omega)\right] &= \lim_{N\to\infty}\frac{1}{N}\left(\sum_{i=1}^{N}\left[C^{\phi}_{ii}(\omega)\right]^2 + \sum_{j\neq i}^{N} C^{\phi}_{ij}(\omega)C^{\phi}_{ij}(-\omega)\right) \\ &= \left[C^{\phi}(\omega)\right]^2 + \psi^{\phi}(\omega) = \frac{\left(1+\omega^2\right)^2}{\left(1 + \omega^2 - g^2\langle\phi'\rangle^2\right)^2}\left[C^{\phi}(\omega)\right]^2,\end{aligned} \tag{B.13}$$

$$\varphi_2\left[\mathbf{C}^{x}(\omega)\right] = \left[C^{x}(\omega)\right]^2 + \psi^{x}(\omega) = \frac{g^4}{\left(1 + \omega^2 - g^2\langle\phi'\rangle^2\right)^2}\left[C^{\phi}(\omega)\right]^2 + \frac{(1+\omega^2)^2 - g^4\langle\phi'\rangle^4}{\left(1 + \omega^2 - g^2\langle\phi'\rangle^2\right)^2}\left[C^{x}(\omega)\right]^2. \tag{B.14}$$

Using Eq. (B.13), we can obtain the frequency-dependent dimension for $\mathbf{C}^{\phi}(\omega)$ (Eq. (3.1) in the main text),

$$D^{\phi}(\omega)=\frac{\varphi_1^2\left[\mathbf{C}^{\phi}(\omega)\right]}{\varphi_2\left[\mathbf{C}^{\phi}(\omega)\right]}=\left(1-\frac{g^2\langle\phi'\rangle^2}{1+\omega^2}\right)$$

Note that the second moment of $\mathbf{C}^{x}(\omega)$ Eq. (B.14) derived here using the two-cavity method matches exactly with Eq. (D.7) obtained using random matrix theory in Appendix D.

# C Scalar factor in $\mathbf{C}^{\phi}(\omega)$ spectrum ansatz

In Section 3, we assume that $\mathbf{C}^{\phi}(\omega)$ has a similar expression as in the case of the linear dynamics when replacing $g$ with the effective $g_{\text{eff}}=g\langle\phi'\rangle$, that is,

$$\mathbf{C}^{\phi}(\omega)=m(\omega)\left(\mathbf{I}-\frac{\langle\phi'\rangle}{1+i\omega}\mathbf{J}\right)^{-1}\left(\mathbf{I}-\frac{\langle\phi'\rangle}{1-i\omega}\mathbf{J}^T\right)^{-1}. \tag{C.1}$$

Here $m(\omega)$ is a scalar function to be determined. Taking the first moment (i.e., normalized trace) of the two sides of Eq. (C.1),

$$\varphi\left[\mathbf{C}^{\phi}(\omega)\right]=\frac{m(\omega)}{1-g^2\langle\phi'\rangle^2/(1+\omega^2)}.$$

Here we have used the random matrix formula $\varphi\left[(\mathbf{I}-z\mathbf{J}_0)^{-1}\left(\mathbf{I}-z^*\mathbf{J}_0^T\right)^{-1}\right]=(1-|z|^2)^{-1}$ for $\mathbf{J}_0$ with i.i.d. $\mathcal{N}(0,1/N)$ entries [11] with $z=\frac{g\langle\phi'\rangle}{1+i\omega}$. This shows that

$$m(\omega)=\left(1-\frac{g^2\langle\phi'\rangle^2}{1+\omega^2}\right)C^{\phi}(\omega),$$

which gives the complete $\mathbf{C}^{\phi}(\omega)$ ansatz Eq. (3.3) in the main text.

# D Random matrix derivation of $\mathbf{C}^{x}(\omega)$ moments and dimension

Here we use random matrix theory to derive the first and second moments of $\mathbf{C}^{x}(\omega)$, which is a different approach from the two-cavity method ([4], Appendix B). Note that all the matrices in this section are by default frequency-dependent, which also means that they are potentially complex valued.

First, we elaborate some steps in deriving Eq. (3.7). In the main text (Section 3.1), we have derived the equations $\mathbf{C}^{x\xi}(\omega)=\frac{1}{1+i\omega}\left[\mathbf{J}\mathbf{C}^{\phi\xi}(\omega)+\sigma^2\mathbf{I}\right]$ and $\mathbf{C}^{\phi\xi}(\omega)=\mathbf{D}_{\langle\phi'\rangle}\mathbf{C}^{x\xi}(\omega)$, from which we can solve for $\mathbf{C}^{\phi\xi}(\omega)$,

$$\mathbf{C}^{\phi\xi}(\omega)=\frac{\sigma^2}{1+i\omega}\left(\mathbf{I}-\frac{1}{1+i\omega}\mathbf{D}_{\langle\phi'\rangle}\mathbf{J}\right)^{-1}\mathbf{D}_{\langle\phi'\rangle}. \tag{D.1}$$

Plugging this and Eq. (3.3) into Eq. (3.4), we get

$$\begin{aligned}\mathbf{C}^{x}(\omega)=&\left(1-\frac{g^2\langle\phi'\rangle^2}{1+\omega^2}\right)\frac{C^{\phi}(\omega)}{1+\omega^2}\mathbf{J}\left(\mathbf{I}-\frac{\langle\phi'\rangle}{1+i\omega}\mathbf{J}\right)^{-1}\left(\mathbf{I}-\frac{\langle\phi'\rangle}{1-i\omega}\mathbf{J}^T\right)^{-1}\mathbf{J}^T\\&+\frac{\sigma^2}{1+\omega^2}\left[\frac{\langle\phi'\rangle}{1+i\omega}\mathbf{J}\left(\mathbf{I}-\frac{\langle\phi'\rangle}{1+i\omega}\mathbf{J}\right)^{-1}+\frac{\langle\phi'\rangle}{1-i\omega}\left(\mathbf{I}-\frac{\langle\phi'\rangle}{1-i\omega}\mathbf{J}^T\right)^{-1}\mathbf{J}^T+\mathbf{I}\right].\end{aligned} \tag{D.2}$$

As usual, here we have invoked the homogeneity of neurons when $N \to \infty$ thus $\mathbf{D}_{\langle \phi' \rangle} = \langle \phi' \rangle \mathbf{I}$. To proceed, we can add a term $\frac{\sigma^2}{1+\omega^2} \frac{\langle \phi' \rangle^2}{1+\omega^2} \mathbf{J} \left( \mathbf{I} - \frac{\langle \phi' \rangle}{1+i\omega} \mathbf{J} \right)^{-1} \left( \mathbf{I} - \frac{\langle \phi' \rangle}{1-i\omega} \mathbf{J}^T \right)^{-1} \mathbf{J}^T$ to the second term in Eq. (D.2) to complete a product. This shows that

$$\begin{aligned} \mathbf{C}^x(\omega) = & \left[ \left( 1 - \frac{g^2 \langle \phi' \rangle^2}{1+\omega^2} \right) \frac{C^\phi(\omega)}{1+\omega^2} - \frac{\sigma^2 \langle \phi' \rangle^2}{(1+\omega^2)^2} \right] \mathbf{J} \left( \mathbf{I} - \frac{\langle \phi' \rangle}{1+i\omega} \mathbf{J} \right)^{-1} \left( \mathbf{I} - \frac{\langle \phi' \rangle}{1-i\omega} \mathbf{J}^T \right)^{-1} \mathbf{J}^T \\ & + \frac{\sigma^2}{1+\omega^2} \left[ \mathbf{I} + \frac{\langle \phi' \rangle}{1+i\omega} \mathbf{J} \left( \mathbf{I} - \frac{\langle \phi' \rangle}{1+i\omega} \mathbf{J} \right)^{-1} \right] \left[ \mathbf{I} + \frac{\langle \phi' \rangle}{1-i\omega} \left( \mathbf{I} - \frac{\langle \phi' \rangle}{1-i\omega} \mathbf{J}^T \right)^{-1} \mathbf{J}^T \right]. \end{aligned}$$

Note that

$$\mathbf{I} + \frac{\langle \phi' \rangle}{1+i\omega} \mathbf{J} \left( \mathbf{I} - \frac{\langle \phi' \rangle}{1+i\omega} \mathbf{J} \right)^{-1} = \left( \mathbf{I} - \frac{\langle \phi' \rangle}{1+i\omega} \mathbf{J} \right)^{-1},$$

and using the single neuron mean-field equation Eq. (2.2),

$$\left( 1 - \frac{g^2 \langle \phi' \rangle^2}{1+\omega^2} \right) \frac{C^\phi(\omega)}{1+\omega^2} - \frac{\sigma^2 \langle \phi' \rangle^2}{(1+\omega^2)^2} = \frac{C^\phi(\omega) - \langle \phi' \rangle^2 C^x(\omega)}{1+\omega^2},$$

we have (Eq. (3.7) in the main text)

$$\begin{aligned} \mathbf{C}^x(\omega) = & \frac{C^\phi(\omega) - \langle \phi' \rangle^2 C^x(\omega)}{1+\omega^2} \mathbf{J} \left( \mathbf{I} - \frac{\langle \phi' \rangle}{1+i\omega} \mathbf{J} \right)^{-1} \left( \mathbf{I} - \frac{\langle \phi' \rangle}{1-i\omega} \mathbf{J}^T \right)^{-1} \mathbf{J}^T \\ & + \frac{\sigma^2}{1+\omega^2} \left( \mathbf{I} - \frac{\langle \phi' \rangle}{1+i\omega} \mathbf{J} \right)^{-1} \left( \mathbf{I} - \frac{\langle \phi' \rangle}{1-i\omega} \mathbf{J}^T \right)^{-1}. \end{aligned}$$

In the following, we first describe some general random matrix results, then apply them to computing $\mathbf{C}^x(\omega)$ moments. Let $\mathbf{J}_0 = \mathbf{J}/g$, whose entries are drawn i.i.d. from $\mathcal{N}(0, 1/N)$. Let $z$ to be a complex number with $|z| < 1$, and denote $\mathbf{B}(z) = (\mathbf{I} - z\mathbf{J}_0)^{-1}$ and $\mathbf{A}(z) = \mathbf{B}(z) - \mathbf{I} = z\mathbf{J}_0 (\mathbf{I} - z\mathbf{J}_0)^{-1}$. We have the following identities in the limit of $N \to \infty$ (recall that $\varphi[\cdot] :=$

$\lim_{N\to\infty}\frac{1}{N}\operatorname{Tr}\langle\cdot\rangle_{\mathbf{J}_0}$):

$$
\begin{aligned}
\varphi\left[z\mathbf{J}_0\right] =& z\varphi\left[\mathbf{J}_0\right]=0,\\
\varphi\left[\mathbf{B}(z)\right] =& \varphi\left[\sum_{n=0}^{\infty}\left(z\mathbf{J}_0\right)^n\right]=1,\\
\varphi\left[\mathbf{A}(z)\right] =& \varphi\left[\sum_{n=1}^{\infty}\left(z\mathbf{J}_0\right)^n\right]=\varphi\left[\mathbf{B}(z)-\mathbf{I}\right]=0,\\
\varphi\left[\mathbf{A}^2(z)\right] =& \varphi\left[\sum_{n=1}^{\infty}nz^{n+1}\mathbf{J}_0^{n+1}\right]=\sum_{n=1}^{\infty}nz^{n+1}\varphi\left[\mathbf{J}_0^{n+1}\right]=0,\\
\varphi\left[\mathbf{B}^2(z)\right] =& \varphi\left[\left(\mathbf{A}(z)+\mathbf{I}\right)^2\right]=\varphi\left[\mathbf{A}^2(z)+2\mathbf{A}(z)+\mathbf{I}\right]=1,\\
\varphi\left[\mathbf{B}(z)\mathbf{B}^\dagger(z)\right] =& \frac{1}{1-|z|^2}\qquad [11],\\
\varphi\left[\mathbf{A}(z)\mathbf{A}^\dagger(z)\right] =& \varphi\left[\mathbf{B}(z)\mathbf{B}^\dagger(z)\right]-\varphi\left[\mathbf{B}(z)+\mathbf{B}^\dagger(z)\right]+\varphi\left[\mathbf{I}\right]=\frac{1}{1-|z|^2}-1=\frac{|z|^2}{1-|z|^2},\\
\varphi\left[\mathbf{A}^2(z)\mathbf{A}^\dagger(z)\right] =& \varphi\left[\left(\sum_{n=1}^{\infty}\left(z\mathbf{J}_0\right)^n\right)^2\left(\sum_{n=1}^{\infty}\left(z\mathbf{J}_0\right)^n\right)^\dagger\right]=\varphi\left[\sum_{n=1}^{\infty}\sum_{m=1}^{\infty}nz^{n+1}\mathbf{J}_0^{n+1}\left(z^m\mathbf{J}_0^m\right)^\dagger\right]\\
=& \sum_{n=1}^{\infty}n\varphi\left[z^{n+1}\mathbf{J}_0^{n+1}\left(z^{n+1}\mathbf{J}_0^{n+1}\right)^\dagger\right]=\sum_{n=1}^{\infty}n|z|^{2n+2}=\frac{|z|^4}{\left(1-|z|^2\right)^2},\\
\varphi\left[\mathbf{B}^2(z)\mathbf{B}^\dagger(z)\right] =& \varphi\left[\left(\mathbf{A}(z)+\mathbf{I}\right)^2\left(\mathbf{A}(z)+\mathbf{I}\right)^\dagger\right]=\varphi\left[\mathbf{A}^2(z)\mathbf{A}^\dagger(z)\right]+\varphi\left[2\mathbf{A}(z)\mathbf{A}^\dagger(z)+\mathbf{A}^2(z)\right]\\
&+\varphi\left[2\mathbf{A}(z)+\mathbf{A}^\dagger(z)+\mathbf{I}\right]=\frac{|z|^4}{\left(1-|z|^2\right)^2}+\frac{2|z|^2}{1-|z|^2}+1=\frac{1}{\left(1-|z|^2\right)^2},\\
\varphi_2\left[\mathbf{B}(z)\mathbf{B}^\dagger(z)\right] =& \varphi\left[\mathbf{B}(z)\mathbf{B}^\dagger(z)\mathbf{B}(z)\mathbf{B}^\dagger(z)\right]=\frac{1}{\left(1-|z|^2\right)^4}\qquad [11].
\end{aligned}
\tag{D.3}
$$

All these moment results are all real valued. We can similarly show the conjugate transpose versions, such as $\varphi\left[\mathbf{A}^\dagger(z)\right]$, $\varphi\left[(\mathbf{A}^\dagger(z))^2\mathbf{A}(z)\right]$, which have the same values as their counterparts above.

To apply to $\mathbf{C}^x(\omega)$, note that $\mathbf{J}_{\mathrm{e}}=\frac{\langle\phi'\rangle}{1+i\omega}\mathbf{J}=\frac{g\langle\phi'\rangle}{1+i\omega}\mathbf{J}_0$, and let $z=\frac{g\langle\phi'\rangle}{1+i\omega}$. The norm $|z|=g_{\mathrm{eff}}(\omega)=g_{\mathrm{eff}}/\sqrt{1+\omega^2}<1$ (Appendix H). Let $m(\omega)=C^\phi(\omega)\left(1-\frac{g^2\langle\phi'\rangle^2}{1+\omega^2}\right)=C^\phi(\omega)[1-g_{\mathrm{eff}}^2(\omega)]$, we can then write Eq. (D.2) as

$$
\mathbf{C}^x(\omega)=\frac{m(\omega)}{\langle\phi'\rangle^2}\mathbf{A}\mathbf{A}^\dagger+\frac{\sigma^2}{1+\omega^2}(\mathbf{A}+\mathbf{A}^\dagger+\mathbf{I}).
\tag{D.4}
$$

## D.1 First moment of $\mathbf{C}^x(\omega)$

Using identities in Eq. (D.3), the first moment of Eq. (D.4) can be computed as,

$$
\varphi_1\left[\mathbf{C}^x(\omega)\right]=\frac{m(\omega)}{\langle\phi'\rangle^2}\frac{g_{\mathrm{eff}}^2(\omega)}{1-g_{\mathrm{eff}}^2(\omega)}+0+0+\frac{\sigma^2}{1+\omega^2}=\frac{g^2C^\phi(\omega)+\sigma^2}{1+\omega^2}.
\tag{D.5}
$$

Note that the left hand side is the (homogeneous) diagonal entry $C^x(\omega)$. The above equation is exactly the same as the single neuron mean-field theory for the autocorrelation function Eq. (2.2).

### D.2 Second moment of $\mathbf{C}^x(\omega)$

We will first focus on the first term in Eq. (D.4), which is the only term when $\sigma = 0$. We have,

$$\begin{aligned}
\varphi_2\left[\mathbf{C}^x(\omega)\right] =& \frac{m^2(\omega)}{\langle\phi'\rangle^4}\varphi\left[\mathbf{A}\mathbf{A}^\dagger\mathbf{A}\mathbf{A}^\dagger\right] = \frac{m^2(\omega)}{\langle\phi'\rangle^4}\varphi\left[(\mathbf{B}-\mathbf{I})(\mathbf{B}-\mathbf{I})^\dagger(\mathbf{B}-\mathbf{I})(\mathbf{B}-\mathbf{I})^\dagger\right] \\
=& \frac{m^2(\omega)}{\langle\phi'\rangle^4}\left(\varphi\left[\mathbf{B}\mathbf{B}^\dagger\mathbf{B}\mathbf{B}^\dagger\right] - 2\varphi\left[\mathbf{B}^2\mathbf{B}^\dagger\right] - 2\varphi\left[\mathbf{B}\left(\mathbf{B}^\dagger\right)^2\right] + \varphi\left[\mathbf{B}^2\right] + \varphi\left[\left(\mathbf{B}^\dagger\right)^2\right]\right. \\
& \left. +4\varphi\left[\mathbf{B}\mathbf{B}^\dagger\right] - 2\varphi\left[\mathbf{B}\right] - 2\varphi\left[\mathbf{B}^\dagger\right] + \varphi(\mathbf{I})\right) \\
=& \frac{m^2(\omega)}{\langle\phi'\rangle^4}\frac{g^4\langle\phi'\rangle^4\left[2-g_{\text{eff}}^4(\omega)\right]}{(1+\omega^2)^2\left[1-g_{\text{eff}}^2(\omega)\right]^4} = \frac{2-g_{\text{eff}}^4(\omega)}{\left[1-g_{\text{eff}}^2(\omega)\right]^2}\left[\frac{g^2C^\phi(\omega)}{1+\omega^2}\right]^2 \\
=& \frac{2-g_{\text{eff}}^4(\omega)}{\left[1-g_{\text{eff}}^2(\omega)\right]^2}\left[C^x(\omega)\right]^2.
\end{aligned} \tag{D.6}$$

Again, we used the random matrix identities in Eq. (D.3) and the single-neuron mean-field identity Eq. (2.2) $g^2C^\phi(\omega) = (1+\omega^2)C^x(\omega)$ for $\sigma = 0$ case.

Next, for the general case with $\sigma \geq 0$, the second moment of $\mathbf{C}^x(\omega)$ involves a few additional terms that can be similarly computed,

$$\begin{aligned}
\varphi_2\left[\mathbf{C}^x(\omega)\right] =& \frac{m^2(\omega)}{\langle\phi'\rangle^4}\varphi\left[\mathbf{A}\mathbf{A}^\dagger\mathbf{A}\mathbf{A}^\dagger\right] + \frac{m(\omega)\sigma^2}{\langle\phi'\rangle^2(1+\omega^2)}\varphi\left[2\mathbf{A}^2\mathbf{A}^\dagger + 2\mathbf{A}\left(\mathbf{A}^\dagger\right)^2 + 2\mathbf{A}\mathbf{A}^\dagger\right] \\
& + \frac{\sigma^4}{(1+\omega^2)^2}\varphi\left[\mathbf{A}^2 + \left(\mathbf{A}^\dagger\right)^2 + 2\mathbf{A}\mathbf{A}^\dagger + 2\mathbf{A} + 2\mathbf{A}^\dagger + \mathbf{I}\right] \\
=& \frac{2-g_{\text{eff}}^4(\omega)}{\left[1-g_{\text{eff}}^2(\omega)\right]^2}\left[\frac{g^2C^\phi(\omega)}{1+\omega^2}\right]^2 + \frac{\sigma^2}{1+\omega^2}\frac{2\left[1+g_{\text{eff}}^2(\omega)\right]}{1-g_{\text{eff}}^2(\omega)}\frac{g^2C^\phi(\omega)}{1+\omega^2} + \frac{\sigma^4}{(1+\omega^2)^2}\frac{1+g_{\text{eff}}^2(\omega)}{1-g_{\text{eff}}^2(\omega)} \\
=& \frac{\frac{g^4}{(1+\omega^2)^2}}{\left[1-g_{\text{eff}}^2(\omega)\right]^2}\left[C^\phi(\omega)\right]^2 + \frac{1-g_{\text{eff}}^4(\omega)}{\left[1-g_{\text{eff}}^2(\omega)\right]^2}\left[C^x(\omega)\right]^2.
\end{aligned} \tag{D.7}$$

Again, we used the single-neuron mean-field identity Eq. (2.2) in the last equality. This result matches exactly with the one derived using the two-cite cavity method (Eq. (B.14)) and the result in [4] when $\sigma = 0$.

Using the first and second moments of $\mathbf{C}^x(\omega)$ (Eqs. (D.5) and (D.7)), we can obtain the frequency dependent dimension of $D^x(\omega)$ (Eq. (3.14) in the main text),

$$\begin{aligned}
D^x(\omega) =& \frac{\varphi_1^2\left[\mathbf{C}^x(\omega)\right]}{\varphi_2\left[\mathbf{C}^x(\omega)\right]} = \frac{\left[C^x(\omega)\right]^2}{\frac{1}{\left[1-g_{\text{eff}}^2(\omega)\right]^2}\left[\frac{g^2C^\phi(\omega)}{1+\omega^2}\right]^2 + \frac{1-g_{\text{eff}}^4(\omega)}{\left[1-g_{\text{eff}}^2(\omega)\right]^2}\left[C^x(\omega)\right]^2} \\
=& \frac{\left[1-g_{\text{eff}}^2(\omega)\right]^2\left[C^x(\omega)\right]^2}{\left[C^x(\omega)-\frac{\sigma^2}{1+\omega^2}\right]^2 + \left[1-g_{\text{eff}}^4(\omega)\right]\left[C^x(\omega)\right]^2} \\
=& \frac{\left[1-g_{\text{eff}}^2(\omega)\right]^2}{1+\left[1-\frac{\sigma^2}{(1+\omega^2)C^x(\omega)}\right]^2 - g_{\text{eff}}^4(\omega)}
\end{aligned}$$

In the special case when $\sigma = 0$, similar to the cancellation when computing $D^\phi(\omega)$, Eq. (3.14)

reduces to a simple expression without explicit dependence on $C^x(\omega)$,

$$D^x(\omega) = \frac{\left[1 - g_{\text{eff}}^2(\omega)\right]^2}{2 - g_{\text{eff}}^4(\omega)} = \frac{\left(1 + \omega^2 - g_{\text{eff}}^2\right)^2}{2\left(1 + \omega^2\right)^2 - g_{\text{eff}}^4}. \tag{D.8}$$

# E Extending $\zeta$ properties to $\sigma \geq 0$ case

In this section, we extend the results on the relationship between $C^\zeta(\omega)$, $C^\phi(\omega)$, and $C^x(\omega)$ in the main text Section 3.2 to the case with external noise input $\sigma \geq 0$. As shown below, $\tilde{\zeta}$ plays a similar role as the external noise input $\xi$ in networks with linear dynamics.

Recall that the total effective noise $\tilde{\zeta}_i$ is

$$\tilde{\zeta}_i(\omega) := \zeta_i(\omega) + \frac{\langle \phi_i' \rangle}{1 + i\omega}\xi_i(\omega) = \phi_i(\omega) - \langle \phi_i' \rangle x_i(\omega) + \frac{\langle \phi_i' \rangle}{1 + i\omega}\xi_i(\omega) = \phi_i(\omega) - \frac{\langle \phi_i' \rangle}{1 + i\omega}\sum_{j=1}^N J_{ij}\phi_j(\omega). \tag{E.1}$$

Here we have used the Fourier transform of the network dynamics Eq. (2.1),

$$x(\omega) = \frac{1}{1 + i\omega}\left[\sum_{j=1}^N J_{ij}\phi_j(\omega) + \xi_i(\omega)\right].$$

From Eq. (E.1), the Fourier transform of firing rate $\phi_i(\omega)$ can be readily solved in terms of $\tilde{\zeta}_j(\omega)$ in the vector form, similarly as Eq. (3.10),

$$\boldsymbol{\phi}(\omega) = \left[\mathbf{I} - \frac{1}{1 + i\omega}\mathbf{D}_{\langle \phi' \rangle}\mathbf{J}\right]^{-1}\tilde{\boldsymbol{\zeta}}(\omega). \tag{E.2}$$

From this, we immediately obtain a general form of Eq. (3.11) where $\mathbf{C}^\zeta(\omega)$ is replaced by $\mathbf{C}^{\tilde{\zeta}}(\omega)$ when $N \to \infty$

$$\mathbf{C}^\phi(\omega) = \left[\mathbf{I} - \mathbf{J}_{\text{e}}\right]^{-1}\mathbf{C}^{\tilde{\zeta}}(\omega)\left[\mathbf{I} - \mathbf{J}_{\text{e}}^\dagger\right]^{-1}. \tag{E.3}$$

Accordingly, the condition (Eq. (3.12)) sufficient to derive the $\mathbf{C}^\phi(\omega)$ ansatz (Eq. (3.3)) is changed to

$$\text{Ansatz:} \quad \mathbf{C}^{\tilde{\zeta}}(\omega) = \left(1 - \frac{g^2\langle \phi' \rangle^2}{1 + \omega^2}\right)C^\phi(\omega) \cdot \mathbf{I} \quad \text{as } N \to \infty. \tag{E.4}$$

To derive Eq. (E.4), note that

$$\mathbf{C}^{\tilde{\zeta}}(\omega) = \mathbf{C}^\zeta(\omega) + \frac{1}{1 - i\omega}\mathbf{C}^{\zeta\xi}(\omega)\mathbf{D}_{\langle \phi' \rangle} + \frac{1}{1 + i\omega}\mathbf{D}_{\langle \phi' \rangle}\mathbf{C}^{\xi\zeta}(\omega) + \frac{1}{1 + \omega^2}\mathbf{D}_{\langle \phi' \rangle}\mathbf{C}^\xi(\omega)\mathbf{D}_{\langle \phi' \rangle}. \tag{E.5}$$

First, we claim that $\mathbf{C}^{\zeta\xi}(\omega) = 0$ (and so is its conjugate transpose $\mathbf{C}^{\xi\zeta}(\omega) = 0$), which is consistent with $\boldsymbol{\zeta}$ and $\boldsymbol{\xi}$ being independent. This zero cross-covariance is because, for any $i, j \in \{1, \cdots, N\}$ and $\tau \in \mathbb{R}$,

$$C_{ij}^{\zeta\xi}(\tau) = \left\langle \left(\phi_i(t) - \langle \phi_i' \rangle x_i(t)\right)\xi_j(t + \tau)\right\rangle = \langle \phi_i(t)\xi_j(t + \tau)\rangle - \langle \phi_i' \rangle \langle x_i(t)\xi_j(t + \tau)\rangle = 0.$$

The last equality above is because of the jointly Gaussian distribution of $(x_i, \xi_j)$ and the Stein's lemma. For the last term in Eq. (E.5), note that $\mathbf{C}^\xi(\omega) = \sigma^2 \cdot \mathbf{I}$ since the external noise is i.i.d.

Finally, we use the ansatz for $\zeta$ (Eq. (3.12)) and the expression of its diagonal entries (Eq. (3.9)). In particular, *the first equally* of Eq. (3.9), $C^{\zeta}(\omega) = C^{\phi}(\omega) - \langle\phi'\rangle^2 C^x(\omega)$, still holds since its derivation does not involve whether $\sigma$ is zero or positive. Therefore Eq. (E.5) becomes (invoking the homogeneity of neurons to write $\langle\phi_i'\rangle = \langle\phi'\rangle$ as $N \to \infty$),

$$\mathbf{C}^{\tilde{\zeta}}(\omega) = \left[C^{\phi}(\omega) - \langle\phi'\rangle^2 C^x(\omega)\right] \cdot \mathbf{I} + 0 + 0 + \frac{\sigma^2 \langle\phi'\rangle^2}{1+\omega^2} \cdot \mathbf{I} = \left(1 - \frac{g^2 \langle\phi'\rangle^2}{1+\omega^2}\right) C^{\phi}(\omega) \cdot \mathbf{I}.$$

We used Eq. (2.2) in the last equal sign.

To obtain Eq. (3.13), again note that the definion of $\zeta$ is unchanged and the first equally of Eq. (3.9) still holds.

# F Asymptotic power law tail of covariance spectra $p^{a,\omega}(\lambda)$

To derive the power law tail approximation, we follow the method in [11], Supplementary Materials B. Briefly, the method assumes that as the parameter $g_{\text{eff}} \to 1^-$, the probability density function of the spectrum $p_{g_{\text{eff}}}(\lambda)$ coverages to a finite, positive value for any fixed $\lambda > \lambda_-^0 \geq 0$ ($\lambda_-^0$ is the limit of the left edge of the spectrum support), and its large value tail follows a power law

$$\lim_{\lambda\to\infty} \lim_{g_{\text{eff}}\to 1^-} \lambda^{\beta} p_{g_{\text{eff}}}(\lambda) = 1,$$

and the right edge of the spectrum's support diverges as $\lambda_+ \propto (1 - g_{\text{eff}}^2)^{-\alpha}$. Then the moments of the spectrum, as orders of $(1 - g_{\text{eff}}^2)$, are determined by the exponents $\alpha$, $\beta$:

$$\mathbb{E}\left[\lambda^n\right] \propto \delta^{-\alpha(-\beta+n+1)}, \quad \delta = (1 - g_{\text{eff}}^2), \tag{F.1}$$

which also means that we can solve for the exponent $\alpha, \beta$ from two moments of the spectrum.

Define

$$m(\omega) = C^{\phi}(\omega)\left(1 - \frac{g^2 \langle\phi'\rangle^2}{1+\omega^2}\right), \text{ and } n(\omega) = \frac{\sigma^2 \langle\phi'\rangle^2}{1+\omega^2}. \tag{F.2}$$

The expression of $\mathbf{C}^x(\omega)$ (Eq. (3.13)) can be written as

$$\langle\phi'\rangle^2 \mathbf{C}^x(\omega) = [m(\omega) - n(\omega)]\, \mathbf{J}_{\text{e}} (\mathbf{I} - \mathbf{J}_{\text{e}})^{-1} \left(\mathbf{I} - \mathbf{J}_{\text{e}}^{\dagger}\right)^{-1} \mathbf{J}_{\text{e}}^{\dagger} + n(\omega) (\mathbf{I} - \mathbf{J}_{\text{e}})^{-1} \left(\mathbf{I} - \mathbf{J}_{\text{e}}^{\dagger}\right)^{-1}. \tag{F.3}$$

This also allows us to consider the asymptotics of the frequency dependent spectrum by considering the limit of

$$g_{\text{eff}}(\omega) = \frac{g \langle\phi'\rangle}{\sqrt{1+\omega^2}} \to 1^-, \quad \text{and the orders of moments in } \delta = (1 - g_{\text{eff}}^2(\omega)),$$

instead of $g_{\text{eff}} \to 1^-$ and $\delta = 1 - g_{\text{eff}}^2(\omega)$.

As a corollary of the diagonal entries of $\mathbf{C}^{\zeta}(\omega)$ (Eq. (3.9), note its first equality is general and valid for $\sigma \geq 0$),

$$0 \leq C^{\zeta}(\omega) = C^{\phi}(\omega) - \langle\phi'\rangle^2 C^x(\omega) = C^{\phi}(\omega) - \frac{\langle\phi'\rangle^2 (g^2 C^{\phi}(\omega) + \sigma^2)}{1+\omega^2}.$$

This leads to an inequality,

$$m(\omega) \geq n(\omega) \geq 0. \tag{F.4}$$

Note that the power law property $p(\lambda) \propto \lambda^{-\beta}$ is invariant when multiplying the covariance matrix/eigenvalues with a scalar. Therefore, we can equivalently focus on deriving a power law for $\tilde{\mathbf{C}}^x(\omega) := \langle\phi'\rangle^2 \mathbf{C}^x(\omega)/m(\omega)$, which is

$$\tilde{\mathbf{C}}^x(\omega) = \left(1 - \frac{n(\omega)}{m(\omega)}\right)\mathbf{P} + \frac{n(\omega)}{m(\omega)}\mathbf{Q}, \tag{F.5}$$

where

$$\mathbf{P} = \mathbf{J}_e(\mathbf{I} - \mathbf{J}_e)^{-1}\left(\mathbf{I} - \mathbf{J}_e^\dagger\right)^{-1}\mathbf{J}_e^\dagger, \quad \mathbf{Q} = (\mathbf{I} - \mathbf{J}_e)^{-1}\left(\mathbf{I} - \mathbf{J}_e^\dagger\right)^{-1}.$$

From the analytical expression for linear dynamics covariance spectrum [11], we know that the spectrum of $\mathbf{Q}$ as $g_{\text{eff}}(\omega) \to 1^-$ has a probability density function $p_{\mathbf{Q}}(\lambda)$ that converge to a finite value for any fixed $\lambda$. For the matrix $\mathbf{P}$, we hypothesize the same is true. The scalar coefficients for $\mathbf{P}$, $\mathbf{Q}$ in Eq. (F.5) are both between 0 and 1 and they sum to 1. Therefore, $\tilde{\mathbf{C}}^x(\omega)$ as the linear combination also satisfies this finite limit property of the spectrum probability density function, and we can thus apply Eq. (F.1) to determine the power law exponent for $\tilde{\mathbf{C}}^x(\omega)$ spectrum.

Using the results from Appendix D

$$\varphi_1\left[\tilde{\mathbf{C}}^x(\omega)\right] = \frac{g_{\text{eff}}^2(\omega)}{1 - g_{\text{eff}}^2(\omega)} + \frac{n(\omega)}{m(\omega)}. \tag{F.6}$$

Since the last term in the above is between 0 and 1, we see that $\varphi_1\left[\tilde{\mathbf{C}}^x(\omega)\right] \propto \delta^{-1}$ as $g_{\text{eff}}(\omega) \to 1^-$. For the second moment (Eq. (D.7)),

$$\varphi_2\left[\tilde{\mathbf{C}}^x(\omega)\right] = \frac{g_{\text{eff}}^4(\omega)}{\left[1 - g_{\text{eff}}^2(\omega)\right]^4} + \left(\frac{g_{\text{eff}}^2(\omega)}{1 - g_{\text{eff}}^2(\omega)} + \frac{n(\omega)}{m(\omega)}\right)^2 \cdot \frac{1 + g_{\text{eff}}^2(\omega)}{1 - g_{\text{eff}}^2(\omega)}. \tag{F.7}$$

As $g_{\text{eff}}(\omega) \to 1^-$, the first term above dominates and hence $\varphi_2\left[\tilde{\mathbf{C}}^x(\omega)\right] \propto \delta^{-4}$. From these moments results, we can solve for the exponents as $\alpha = 3$ and $\beta = -5/3$, which means $\mathbf{C}^x(\omega)$ spectrum has a power law tail as $p^x(\lambda;\omega) \propto \lambda^{-5/3}$.

# G The left edge of $p^x(\lambda;\omega)$'s support when $\sigma = 0$

Starting from the expression of the frequency-dependent covariance matrix of currents (Eq. (3.7), for any fixed $\omega$) at $\sigma = 0$,

$$\mathbf{C}^x(\omega) \propto \mathbf{J}_e(\mathbf{I} - \mathbf{J}_e)^{-1}\left(\mathbf{I} - \mathbf{J}_e^\dagger\right)^{-1}\mathbf{J}_e^\dagger =: \tilde{\mathbf{C}}^x(\omega).$$

Recall that $\mathbf{J}_e = \frac{\langle\phi'\rangle}{1+i\omega}\mathbf{J}$ (Eq. (3.11)) and we introduced $\tilde{\mathbf{C}}^x(\omega)$, differing with $\mathbf{C}^x(\omega)$ by a scalar, for ease of notation (it is the same as Eq. (F.5) while setting $\sigma = 0$). Note that it is sufficient to show that the left edge of spectrum support of $\tilde{\mathbf{C}}^x(\omega)$ being 0.

Since $\tilde{\mathbf{C}}^x(\omega)$ is Hermitian, its minimal eigenvalue is given by

$$\lambda_{\min}\left[\tilde{\mathbf{C}}^x(\omega)\right] = \min_{\|\boldsymbol{v}\|=1} \boldsymbol{v}^\dagger \tilde{\mathbf{C}}^x(\omega)\boldsymbol{v} = \min_{\|v\|=1} \left\|\left(\mathbf{I} - \mathbf{J}_e^\dagger\right)^{-1}\mathbf{J}_e^\dagger \boldsymbol{v}\right\|^2. \tag{G.1}$$

Here the minimization is taken over all vectors $\boldsymbol{v} \in \mathbb{C}^N$, and $\|v\| = \sqrt{\sum_{i=1}^N |v_i|^2}$ is the vector 2-norm. Note that

$$\min_{\|\boldsymbol{v}\|=1} \left\|\mathbf{J}_e^\dagger \boldsymbol{v}\right\| = \frac{\langle\phi'\rangle}{\sqrt{1+\omega^2}} \cdot \min_{\|\boldsymbol{v}\|=1} \|\mathbf{J}^T \boldsymbol{v}\|,$$

and $\min_{\|\boldsymbol{v}\|=1} \left\|\mathbf{J}^T\boldsymbol{v}\right\|$ is the minimal singular value of $\mathbf{J}^T$. Since $J_{ij}$ are i.i.d. Gaussian distributed (Eq. (2.1)), from the well-known Marchenko-Pastur law, the minimal singular value of $\mathbf{J}^T$ is 0. This means that in large networks $N \to \infty$, for any $\delta > 0$, there exists a vector $\boldsymbol{v}_0$ (the minimal singular vector of $\mathbf{J}^T$) such that

$$\|\mathbf{J}^T\boldsymbol{v}_0\| \leq \delta.$$

Consider this special $\boldsymbol{v}_0$ in Eq. (G.1), we have

$$\begin{aligned}\lambda_{\min}\left[\tilde{\mathbf{C}}^x(\omega)\right] &\leq \frac{\langle\phi'\rangle^2}{1+\omega^2}\cdot\left\|\left(\mathbf{I}-\mathbf{J}_{\mathrm{e}}^{\dagger}\right)^{-1}\mathbf{J}^T\boldsymbol{v}_0\right\|^2 \leq \frac{\langle\phi'\rangle^2}{1+\omega^2}\cdot\left\|\left(\mathbf{I}-\mathbf{J}_{\mathrm{e}}^{\dagger}\right)^{-1}\right\|^2\left\|\mathbf{J}^T\boldsymbol{v}_0\right\|^2 \\ &\leq \frac{\delta^2\langle\phi'\rangle^2}{1+\omega^2}\cdot\left\|\left(\mathbf{I}-\mathbf{J}_{\mathrm{e}}^{\dagger}\right)^{-1}\right\|^2.\end{aligned} \tag{G.2}$$

Note that $\left\|(\mathbf{I}-\mathbf{J}_{\mathrm{e}}^{\dagger})^{-1}\right\|^2$ (the operator norm or matrix 2-norm) is the square of the largest singular value of $(\mathbf{I}-\mathbf{J}_{\mathrm{e}}^{\dagger})^{-1}$, which is also the largest eigenvalue of $\left(\mathbf{I}-\frac{\langle\phi'\rangle}{1+i\omega}\mathbf{J}\right)^{-1}\left(\mathbf{I}-\frac{\langle\phi'\rangle}{1-i\omega}\mathbf{J}^T\right)^{-1}$. Using the covariance spectrum expression for networks with linear dynamics [11], in particular its right edge of support, we know that

$$\begin{aligned}&\lambda_{\max}\left[\left(\mathbf{I}-\frac{\langle\phi'\rangle}{1+i\omega}\mathbf{J}\right)^{-1}\left(\mathbf{I}-\frac{\langle\phi'\rangle}{1-i\omega}\mathbf{J}^T\right)^{-1}\right] \\ &= \frac{2+5g_{\mathrm{eff}}^2(\omega)-\frac{g_{\mathrm{eff}}^4(\omega)}{4}+\frac{g_{\mathrm{eff}}(\omega)}{4}\left[8+g_{\mathrm{eff}}^2(\omega)\right]^{3/2}}{2\left[1-g_{\mathrm{eff}}^2(\omega)\right]^3} \leq \frac{7}{\left[1-g_{\mathrm{eff}}^2(\omega)\right]^3}.\end{aligned} \tag{G.3}$$

Here

$$g_{\mathrm{eff}}(\omega) = \frac{\langle\phi'\rangle}{\sqrt{1+\omega^2}}\cdot g \leq g_{\mathrm{eff}} < 1.$$

The last inequality is proved in Appendix H.

In particular, this means $\left\|(\mathbf{I}-\mathbf{J}_{\mathrm{e}}^{\dagger})^{-1}\right\|^2$ is bounded by a fixed number depending only on $g_{\mathrm{eff}}(\omega)$ in large networks $N \to \infty$. Going back to Eq. (G.2), we have

$$\lambda_{\min}\left[\tilde{\mathbf{C}}^x(\omega)\right] \leq \frac{7\delta^2\langle\phi'\rangle^2}{(1+\omega^2)\left[1-g_{\mathrm{eff}}^2(\omega)\right]^3} \leq \frac{7\delta^2}{\left[1-g_{\mathrm{eff}}^2(\omega)\right]^3}.$$

Since $\delta$ can be any positive number and $\tilde{\mathbf{C}}^x(\omega)$ is positive semi-definite so all its eigenvalues are non-negative, this means that $\lambda_{\min} = 0$, that is, the left edge of the support of $\tilde{\mathbf{C}}^x(\omega)$'s spectrum is 0, when there is no external noise $\sigma = 0$.

# H Proof of $g_{\mathrm{eff}} < 1$

Here we prove that the effective connection strength $g_{\mathrm{eff}} < 1$ for all values of $g$ and $\sigma > 0$. Recall that (Eq. (3.9), whose first equality holds generally for $\sigma \geq 0$)

$$C^{\zeta}(\omega) = C^{\phi}(\omega) - \left\langle\phi'\right\rangle^2 C^x(\omega) \geq 0.$$

Multiplying both sides by $g^2$,

$$g_{\mathrm{eff}}^2 = g^2\left\langle\phi'\right\rangle^2 \leq \frac{g^2C^{\phi}(\omega)}{C^x(\omega)} = \frac{(1+\omega^2)C^x(\omega)-\sigma^2}{C^x(\omega)} \leq 1+\omega^2-\frac{\sigma^2}{C^x(\omega)}. \tag{H.1}$$

We have used Eq. (2.2) in the second equality above. The division by $C^x(\omega)$ is justified because $C^x(\omega) \geq \sigma^2/(1+\omega^2) > 0$ (Eq. (2.2)). Since Eq. (H.1) holds for any $\omega$, setting $\omega = 0$ gives $g_{\text{eff}} < 1$.

For the special case without noise $\sigma = 0$ and $g > 1$ (so that the dynamics is not at a fixed point), the above proof can adapted to prove a weaker result $g_{\text{eff}} \leq 1$. In particular, we need to justify $C^x(\omega = 0) > 0$ for the step of dividing it in Eq. (H.1). As shown in [26], $C^x(\tau)$ decreases monotonically to zero with the time lag $\tau$, and hence $C^x(\omega = 0) = \int_{-\infty}^{\infty} C^x(\tau) d\tau$ has no cancellation in the integral and is therefore positive. Lastly, although our proof only shows $g_{\text{eff}} \leq 1$ for $\sigma = 0$, one can directly verify that $g_{\text{eff}} < 1$ and decreases monotonically with $g$ (Fig. S5) by numerically solving the single-neuron mean-field theory Eq. (2.2).

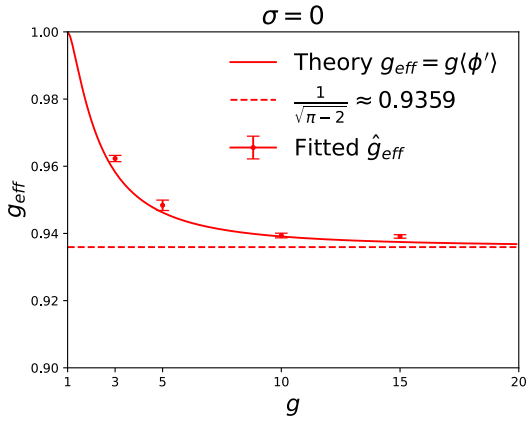


Figure S5: Numerical verification of the strict inequality $g_{\text{eff}} < 1$ for the special case of no noise $\sigma = 0$. The $g_{\text{eff}} = g\langle\phi'\rangle$ decreases from 1 monotonically with $g$ in the chaotic regime $g > 1$. The solid curve is from the mean-field theory (Eq. (2.2) and [24]) and the dots (mean) and error bars (standard error across five $\mathbf{J}$ realizations) show the fitted $\hat{g}_{\text{eff}}$ from network simulations (Eq. (2.1))

# I Proof of non-negative dimension gap $\Delta D(\omega) = D^{\phi}(\omega) - D^x(\omega)$

Here we provide a prove that for the frequency-dependent dimensions, the dimension gap $\Delta D(\omega) = D^{\phi}(\omega) - D^x(\omega)$ is always non-negative for all frequency and is valid for all parameters $g$ and $\sigma$, as long as the dynamics is not at a fixed point (when $\sigma = 0$ and $g < 1$).

We start from Eq. (3.14),

$$D^x(\omega) = \frac{\left(1 + \omega^2 - g^2 \langle\phi'\rangle^2\right)^2}{(1+\omega^2)^2 + \left(1 + \omega^2 - \frac{\sigma^2}{C^x(\omega)}\right)^2 - g^4 \langle\phi'\rangle^4}.$$

Using Eq. (2.2), the second term in the denominator can be written as

$$\left(\frac{(1+\omega^2)C^x(\omega) - \sigma^2}{C^x(\omega)}\right)^2 = \left(\frac{g^2 C^{\phi}(\omega)}{C^x(\omega)}\right)^2 \geq g^4 \langle\phi'\rangle^4.$$

The last inequality is due to $C^{\zeta}(\omega) = C^{\phi}(\omega) - \langle\phi'\rangle^2 C^x(\omega) \geq 0$ (Eq. (3.9) in the main text), since $C^{\zeta}(\omega)$ is the Fourier transform of the autocorrelation function of $\zeta_i$. Using this inequality in the

$D^x(\omega)$ expression,

$$D^x(\omega) \leq \frac{\left(1+\omega^2-g^2\left\langle\phi'\right\rangle^2\right)^2}{\left(1+\omega^2\right)^2} = \left(1-\frac{g^2\left\langle\phi'\right\rangle^2}{1+\omega^2}\right)^2 = D^\phi(\omega),$$

which proves the desired dimension gap. The last equality above is according to Eq. (3.1).

# J Zero time lag dimension and spectrum

The zero time lag dimensions $D^{a,\tau}$, $a \in \{x, \phi\}$ can be computed numerically from the frequency-dependent four point functions derived in Appendix B similarly as the noiseless case $\sigma = 0$ in [4]. Here we describe the key steps for completeness.

By definition using the matrix trace, $D^{a,\tau}$ can be written by separating into diagonal and off-diagonal terms,

$$D^{a,\tau} = \frac{(C^{a,\tau})^2}{(C^{a,\tau})^2 + \psi^{a,\tau}}. \tag{J.1}$$

For the diagonal terms, $C^{x,\tau} = \langle x(t)x(t)\rangle =: c_0$, $C^{\phi,\tau} = \langle\phi(x(t))\phi(x(t))\rangle = \int_{-\infty}^{\infty}\frac{1}{\sqrt{2\pi}}\left[\phi\left(\sqrt{c_0}z\right)\right]^2 e^{-\frac{z^2}{2}}dz$ (recall that $x(t)$ is a Gaussian process as $N \to \infty$), and $c_0$, $C^\phi(\tau)$, $C^x(\tau)$ can be determined by numerically solving the single-neuron mean-field theory Eq. (2.2) as in [24].

The off-diagonal term in Eq. (J.1) is given by the time-lag four point function

$$\psi^{a,\tau} = N\left\langle C^a_{ij}(\tau=0)C^a_{ij}(\tau=0)\right\rangle_{\mathbf{J}}\Big|_{i\neq j}.$$

It can be obtained by (numerically) taking the 2D inverse Fourier Transform of the frequency-dependent four point function $\psi^a(\omega_1, \omega_2)$, which has been derived for the general case of $\sigma \geq 0$ in Appendix B, as Eqs. (B.11) and (B.12).

The asymptotic values of $D^{a,\tau}$ as $g \to \infty$ can be derived based on an analysis of the asymptotic version of the single-neuron mean-field theory Eq. (2.2) discussed in [1] and computed in similarly as in [4]. In particular, $C^x(\tau) = O(g^2)$ and $C^\phi(\tau) = O(1)$, so we can drop the $\sigma^2$ term in Eq. (2.2), when $g \to \infty$ while fixing $\sigma$. This means that we can solve for the diagonal term quantities, $c_0$, $C^\phi(\tau)$, and $C^x(\tau)$ in Eq. (J.1), from the asymptotic version of Eq. (2.2) in [1], their results will be exactly the same as the case when $\sigma = 0$. For the off-diagonal terms, we can use the asymptotic version of Eq. (2.2), $g^2C^\phi(\omega) = (1+\omega^2)C^x(\omega)$ (same as setting $\sigma = 0$), to combine the two terms in Eq. (B.12), which gives

$$\psi^x(\boldsymbol{\omega}) = \left[\frac{2\left|X(\boldsymbol{\omega})\right|^2 - g^4\left\langle\phi'\right\rangle^4}{\left|X(\boldsymbol{\omega}) - g^2\left\langle\phi'\right\rangle^2\right|^2} - 1\right] C^x(\omega_1)C^x(\omega_2).$$

Observe that the above four-point function for currents and the four-point function for rates Eq. (B.11) only depend on $g_{\text{eff}} = g\left\langle\phi'\right\rangle$, $C^\phi(\omega)$, and $C^x(\omega)$, where their asymptotic values do not dependent on $\sigma$. Therefore, the asymptotic dimensions are found to be $\lim_{g\to\infty} D^{x,\tau} \approx 0.0602$, $\lim_{g\to\infty} D^{\phi,\tau} \approx 0.126$, the same as those in [4] for any fixed $\sigma \geq 0$.

The zero time lag covariance spectra $p^{a,\tau}(\lambda)$, $a \in \{x, \phi\}$ is computed from the frequency-dependent covariance matrix theory using a Monte Carlo method. First, we compute $\mathbf{C}^{\phi,\tau}$, $\mathbf{C}^{x,\tau}$ using an entry-wise inverse Fourier transform of the frequency-dependent covariance matrices,

Eqs. (3.3) and (3.7), for a large $N$ and a given realization of the random $\mathbf{J}$. More specifically, $C_{ij}^{a,\tau} = C_{ij}^{a}(\tau = 0) = \frac{1}{2\pi}\int_{-\infty}^{\infty} C_{ij}^{a}(\omega)d\omega$, and we computed it simply by a summation $\mathbf{C}^{a,\tau} = \frac{\Delta\omega}{2\pi}\sum_{k=-K}^{K}\mathbf{C}^{a}(k\Delta\omega)$. In our numerics, $\Delta\omega = 0.1$, $K = 200$ are sufficient to achieve a good matching with the network simulations (Fig. S1BC). After getting $\mathbf{C}^{\phi,\tau}$, $\mathbf{C}^{x,\tau}$, we compute their eigenvalues to get the zero time lag spectrum $p^{a,\tau}(\lambda)$. To improve the accuracy of the spectrum, the process is repeated for multiple $\mathbf{J}$ realizations and the spectra are averaged. One numerical consideration to note is that the network size $N$ needs to be set larger when $g_{\text{eff}}$ is closer to 1, especially to resolve the large right edge of the spectrum support in such cases. For example, while $N = 2000$ and 50 realizations of $\mathbf{J}$ for Fig. S1C is sufficient, we use $N = 10000$ and 10 realizations for Fig. S1B.

## K Time-sampled theoretical spectrum

As noted in [11], when the number of time samples $N_T$ or recording length of neural activity is not substantially larger than the number of neurons $N$ in the network, the effect due to finite time samples on the spectrum and dimension cannot be neglected. To address this, we can extend the theory for the covariance spectrum to the time-sampled case following the method in [11].

The method in [11] assumes that the neural activity $\boldsymbol{x}(t)$ follow a multivariate Gaussian distribution, the sampled covariance matrix $\hat{\mathbf{C}}^{x}$ has the same eigenvalues as $\mathbf{C}^{x}\mathbf{Z}\mathbf{Z}^{T}$, where $\mathbf{C}^{x}$ is the exact covariance matrix and $Z_{ij}$ is drawn i.i.d. from $\mathcal{N}(0, 1/N_T)$. For the firing rates $\boldsymbol{\phi}$, since its covariance (Eq. (3.3)) has the same form as case with linear dynamics, the analytical time-sampled spectrum result in [11] can be directly used to obtain the time-sampled $p^{\phi}(\lambda;\omega)$ by replacing the $g$ with $g_{\text{eff}}(\omega) = \frac{g\langle\phi'\rangle}{\sqrt{1+\omega^2}}$ (Eq. (4.3)). This time-sampled spectrum $p^{\phi}(\lambda;\omega)$ was used in Fig. 2C-F and Fig. S1A, and for fitting $g_{\text{eff}}$ in Fig. 3B. Note that although the multivariate Gaussian distribution assumption may not hold for nonlinear dynamics, the time-sampled spectrum results obtained above are still valid in large networks, as shown in our numerics, thanks to a certain universality phenomenon in random matrix theory.

For the currents $\boldsymbol{x}$, according to the above discussion and Eq. (3.13), the following matrix has the same eigenvalues as the sampled covariance $\hat{\mathbf{C}}^{x}(\omega)$

$$\mathbf{C}^{x}(\omega) = \frac{C^{\zeta}(\omega)}{\langle\phi'\rangle^{2}}\mathbf{J}_{\text{e}}\left(\mathbf{I}-\mathbf{J}_{\text{e}}\right)^{-1}\mathbf{Z}\mathbf{Z}^{T}\left(\mathbf{I}-\mathbf{J}_{\text{e}}^{\dagger}\right)^{-1}\mathbf{J}_{\text{e}}^{\dagger} + \frac{\sigma^{2}}{1+\omega^{2}}\left(\mathbf{I}-\mathbf{J}_{\text{e}}\right)^{-1}\mathbf{Z}\mathbf{Z}^{T}\left(\mathbf{I}-\mathbf{J}_{\text{e}}^{\dagger}\right)^{-1}. \tag{K.1}$$

This allows us to modify the Monte Carlo method for computing the spectrum $p^{x}(\lambda;\omega)$ (Section 4) to obtain the time-sampled spectrum, and it was used in Fig. 2C-F and Fig. S1A.

For dimension, the time-sampled theory in [11] is general and applies to any covariance matrix. In particular, the dimension of the sample covariance matrix $\hat{D}$ is adjusted from the exact covariance dimension $D$ by $\hat{D} = \frac{D}{1+\gamma D}$ with $\gamma = N/N_T < 1$. We used this time-sampled dimension in Fig. 4BD and Fig. S4.

## L Network simulation and additional numerical details

The network model Eq. (2.1) is simulated with first order finite difference method (i.e., the Euler–Maruyama method),

$$x_i(t+\Delta t) = (1-\Delta t)\,x_i(t) + \Delta t\sum_{j=1}^{N} J_{ij}\phi_j(t) + \sqrt{\Delta t}\xi_i(t). \tag{L.1}$$

The external input, $\xi_i(t)$, modeled as white noise is drawn i.i.d. from the Gaussian distribution $\mathcal{N}\left(0, \sigma^2\right)$. The random connectivity $\mathbf{J}$ is drawn and fixed at the beginning of the simulation. To match exactly with the mean-field theory, one would need $N \to \infty$, $\Delta t \to 0$, and the total simulation time $T \to \infty$. We have chosen the simulation parameters balancing computational cost as listed in Table S1 for all figures. In general, $N \sim 10^3$, $T \sim 100N$, and time step $\Delta t = 0.1$ is sufficient to achieve high accuracy.

The time-lagged covariance matrix $\mathbf{C}^{\phi}(\tau)$ is computed from the simulated activity as

$$C_{ij}^{\phi}(\tau) = \frac{\Delta t}{T-\tau} \sum_{k=1}^{\frac{T-\tau}{\Delta t}} \phi_i(t_k)\phi_j(t_k+\tau), \tag{L.2}$$

where $\tau = m\Delta t$, for $m = -M, \cdots, M$. The boundary of the time lags, $\tau_{\max} = M\Delta t$, is chosen to ensure the correlation functions have essentially vanished at that point, similar for $\mathbf{C}^{x}(\tau)$.

To compute the frequency-dependent covariance matrix, $C^a(\omega)$, we first choose a large time bin width $t_{\text{bin}}$, where the correlation function has decayed to be sufficiently small, usually $t_{\text{bin}} = 100$. The total simulation time $T$ is devided into $N_{\text{bin}} = T/t_{\text{bin}}$ intervals. We compute the Fourier transform on the $n$-th interval as $a_i^{(n)}(\omega) = \frac{1}{\sqrt{t_{\text{bin}}}} \int_{(n-1)t_{\text{bin}}}^{nt_{\text{bin}}} a_i(t)dt$ with $a \in \{x, \phi\}$. Then, $C_{ij}^a(\omega) = \frac{1}{N_{\text{bin}}} \sum_{n=1}^{N_{\text{bin}}} a_i^{(n)}(\omega) a_j^{(n)}(-\omega)$ (Note that $a_j^{(n)}(-\omega)$ is the complex conjugate of $a_j^{(n)}(\omega)$). The cross-covariance matrices such as $\mathbf{C}^{\phi x}(\omega) = \frac{1}{N_{\text{bin}}} \sum_{n=1}^{N_{\text{bin}}} \phi_i^{(n)}(\omega) x_j^{(n)}(-\omega)$ are computed similarly.

| Figure | $g$ | $\sigma$ | $N$ | $T$ | $t_{\text{bin}}$ | $\Delta t$ | $\omega$ |
|---|---|---|---|---|---|---|---|
| Fig. 1ABEF | 5 | 0.495 | 10000 | 200N | 100 | 0.1 | 0 |
| Fig. 1CD | 5 | 0.495 | 500, 1000, 2000, 3000, 6000, 10000 | 200N | 100 | 0.1 | 0 |
| Fig. 2BE | 5 | 0.495 | 10000 | 200N | 100 | 0.1 | 0 |
| Fig. 2C | 1.7 | 1 | 4000 | 200N | 100 | 0.02 | 0 |
| Fig. 2D | 0.4 | 0.495 | 3000 | 200N | 100 | 0.1 | 0 |
| Fig. 2F | 10 | 0 | 4000 | 3200N | 100 | 0.1 | 0 |
| Fig. 3B | 0.4, 0.9, 1.2, 1.37, 1.5, 2, 3, 5 | 0.495 | 3000 | 200N | 100 | 0.1 | 0 |
| Fig. 4A | 2, 4, 6, 8, 10, 12, 14, 16, 18, 20 | 0 | 4000 (5 realizations) | 50000 | – | 0.1 | – |
| Fig. 4B | 3, 5, 10, 15 | 0 | 2000 (30 realizations) | 200N | 100 | 0.1 | 0 |
| Fig. 4C | 0.4, 0.6, 0.9, 1.1, 1.37, 1.5, 2, 5 | 0.495 | 2000 (5 realizations) | 200N | – | 0.1 | – |
| Fig. 4D | 0.4, 0.6, 0.9, 1.1, 1.37, 1.5, 2, 5 | 0.495 | 2000 (5 realizations) | 200N | 100 | 0.1 | 0 |
| Fig. S1A | 5 | 0.495 | 2000 | 200N | 100 | 0.1 | 0.2 |
| Fig. S1B | 5 | 0.495 | 10000 | 200N | – | 0.1 | – |
| Fig. S1C | 0.4 | 0.495 | 2000 | 200N | – | 0.02 | – |
| Fig. S2A | 0.8 | 0.495 | 4000 (50 realizations) | – | – | – | 0 |
| Fig. S2B | 5 | 0.495 | 4000 (50 realizations) | – | – | – | 0.9 |
| Fig. S2C | 5 | 0 | 4000 (50 realizations) | – | – | – | 0.9 |
| Fig. S3A | 0.4, 0.9, 1.2, 1.37, 1.5 | 0.495 | 3000 | 200N | – | 0.1 | – |
| Fig. S3B | 0.4, 0.9, 1.2, 1.37, 1.5 | 0.495 | 3000 | 200N | 100 | 0.1 | 0 |
| Fig. S3C | 0.4, 0.9, 1.5, 2, 3 | 1 | 3000 | 200N | – | 0.1 | – |
| Fig. S3D | 0.4, 0.9, 1.5, 2, 3 | 1 | 3000 | 200N | 100 | 0.1 | 0 |
| Fig. S4A-D | 3, 15 | 0 | 100, 200, 500, 1000, 2000 | 200N | 100 | 0.1 | 0 |

Table S1: Additional parameters used in the figures. Those that do not apply are marked with "–".